The Impact of Solar Activity on Forecasting the Upper Atmosphere via Assimilation of Electron Density Data

Timothy Kodikara[1] , **Kefei Zhang[2,3]** , **Nicholas Michael Pedatella[4,5]** , **and Claudia Borries[1]**

[1]Institute of Solar-Terrestrial Physics, German Aerospace Center, Neustrelitz, Germany, [2]SPACE Research Centre, RMIT University, Melbourne, VIC, Australia, [3]School of Environment Science and Spatial Informatics, China University of Mining and Technology, Xuzhou, China, [4]High Altitude Observatory, National Center for Atmospheric Research, Boulder, CO, USA, [5]COSMIC Program Office, University Corporation for Atmospheric Research, Boulder, CO, USA

Abstract This study presents a comprehensive comparison of the impact of solar activity on forecasting the upper atmosphere through assimilation of radio occultation (RO)-derived electron density (*Ne*) into a physics-based model (TIE-GCM) using an ensemble Kalman filter (KF). Globally abundant RO-derived *Ne* offers one of the most promising means to test the effect of assimilation on the model forecasted state on a global scale. This study emphasizes the importance of understanding how the assimilation results vary with solar activity, which is one of the main drivers of thermosphere-ionosphere dynamics. This study validates the forecast states with independent RO-derived GRACE (Gravity Recovery and Climate Experiment mission) *Ne* data. The principal result of the study is that the agreement between forecast *Ne* and data is better during solar minimum than solar maximum. The results also show that the agreement between data and forecast is mostly better than that of the standalone TIE-GCM driven with observed geophysical indices. The results emphasize that TIE-GCM significantly underestimate *Ne* in altitudes below 250 km and the assimilation of *Ne* is not as effective in these lower altitudes as it is in higher altitudes. The results demonstrate that assimilation of *Ne* significantly impacts the neutral mass density estimates via the KF state vector—the impact is larger during solar maximum than solar minimum relative to a control case that does not assimilate *Ne*. The results are useful to explain the inherent model bias, to understand the limitations of the data, and to demonstrate the capability of the assimilation technique.

1. Introduction

More studies on data-guided forecasting of the upper atmosphere (thermosphere-ionosphere) are conducted during the past decade than any other time (e.g., Chartier et al., 2016; Codrescu et al., 2018; Elvidge et al., 2016; Hsu et al., 2014; Lee et al., 2012; Sutton, 2018, and references therein). Yet the major thematic issues with forecasting the upper atmosphere remain a scientific, computing and resource challenge. These challenges include, for example, scientific—the problem of physics of the thermosphere-ionosphere system being not fully understood; computing—the problem of developing computationally efficient, operationally viable, and high-accuracy output feedback (nowcast/forecast) assimilation algorithms; and resource—the problem of scarcity of impactful measurements of the system. The forecasting capabilities of the current models of the upper atmosphere are limited and often fall short of precision application requirements such as satellite orbit and space weather prediction (e.g., National Research Council, 2013; Mehta et al., 2018; Sutton, 2018). In physics-based models, this mainly translates into a problem of forecasting the upper atmospheric drivers (solar and geomagnetic activity, and forcing from the lower atmosphere) and—to a lesser extent, an initial value problem due to the significant internal chemistry and dynamics (Pedatella et al., 2018, and references therein). Data assimilation techniques represent a possible pathway to address these challenges and improve both forecasting accuracy and lead-time.

Data-guided forecasting refers to the process of computing the best possible estimate of the state of the system using data along with a numerical prediction of the model state. Lee et al. (2012) and Matsuo et al. (2013) demonstrated early success in affecting the model state in thermosphere-ionosphere-electrodynamics general circulation model (TIE-GCM; Richmond et al., 1992) through an ensemble Kalman filter-based (EnKF) data assimilation technique (Evensen, 1994). The EnKF, compared to the traditional Kalman filter (KF; Kalman, 1960) allows one to bypass some of the limitations that are usually associated with

a large complex nonlinear model such as TIE-GCM (see Evensen, 1994, and references therein). The EnKF is a stochastic Monte-Carlo approximation of the solution to the KF. EnKF algorithms can be designed to gain significant computational efficiency for a given large geophysical model by representing model error covariance through a sample covariance computed from a series (*ensemble*) of model runs. This computational efficiency is partly due to the fact that the size of the model error covariance matrix in EnKF depends on the size of the ensemble and not the size of the model dimensions (e.g., grid space, variables).

A number of other variants of KF-based assimilation techniques and other inductive/deductive techniques, such as three-/four-dimensional variational analysis and optimal interpolation exist (e.g., Daley, 1993; Kalnay, 2002), and have been applied in upper atmospheric data assimilation experiments. For example, Mehta et al. (2018) proposed a reduced order model (ROM) data assimilation framework for neutral mass density (ρ) based on the proper orthogonal decomposition dimensionality reduction technique using TIE-GCM as the base model. A key advantage of the ROM with data assimilation is the reduced computational burden while maintaining the model performance in the absence of data (Mehta et al., 2018). The ROMs usually require training with data that span long periods (e.g., solar cycle) and inherit some of the limitations of the base model (e.g., systematic biases, unmodeled dynamics). The accuracy of the forecasts in the ROM framework is also dependent on the accuracy of the forecasts of the upper atmospheric drivers. Sutton (2018) proposed a data assimilation framework for TIE-GCM based on a compact variational technique where the geophysical indices $F_{10.7}$ solar flux and *Kp* (hereinafter GPIs) are estimated iteratively, and the model is iteratively run until data-model convergence is achieved with these newly estimated driver parameters. This approach recognizes the importance of the drivers represented by the GPIs and preserves the self-consistency of the model by not artificially modifying the internal state of the model. While the results in these studies show promise, the results also convey that applying these techniques to forecast the ionosphere-thermosphere system is not necessarily simplistic.

Globally abundant radio occultation (RO)-derived electron density (*Ne*) is one of the most promising means to test the effect of assimilation on the model forecasted state on a global scale. This work is presented as an extension to Lee et al. (2012); Matsuo et al. (2013), and Hsu et al. (2014). The data assimilation experiments presented in this work use *Ne* profiles from the joint USA-Taiwan Constellation Observing System for Meteorology, Ionosphere, and Climate/Formosa Satellite 3 (COSMIC/FORMOSAT-3; hereinafter COSMIC) mission. Lee et al. (2012) using COSMIC-*Ne* profiles and Hsu et al. (2014) and Matsuo et al. (2013) using synthetic COSMIC data showed that EnKF-based assimilation schemes can effectively adjust TIE-GCM to be more consistent with data. They focused on assimilating over a period of 24 h under solar minimum conditions. Hsu, Matsuo, and Liu (2018) and Hsu, Matsuo, Yue, et al. (2018) presented observing system simulation experiments (OSSEs) of assimilation of synthetic data that represent both COSMIC and the follow-on mission COSMIC-2. Although OSSE results from Hsu, Matsuo, and Liu (2018) covered 1 day each in 2009 and 2013, the model ensembles for both these periods were drawn from similar solar activity levels.

In contrast to previous similar experiments, the main focus of this work is to investigate the impact of solar activity on the assimilation of COSMIC-*Ne* into TIE-GCM. This is accomplished with publicly available data with their typical noise and inhomogeneous spatiotemporal distribution as opposed to synthetic data whose error distribution is usually fitted to a Gaussian distribution. This work also seeks to understand the impact of assimilation of COSMIC-*Ne* on neutral mass density in the thermosphere. The present work investigates the impact of the assimilation by altitude, latitude, and local time, and provides detailed statistics of the performance of the forecast and analysis states.

2. Data and Models

This study assimilates COSMIC-*Ne* profiles into TIE-GCM and validates the assimilation results using RO-derived electron density profiles from the Gravity Recovery and Climate Experiment (GRACE) mission. The GPS RO events with the satellites in these two missions enable the derivation of their respective electron density profiles. The number of successful RO events is proportional to, among others, the number of GPS signal transmitters. Tsai et al. (2001) describe the derivation of electron density from RO data. Liu et al. (2009) and Yue et al. (2010) discuss the errors in the retrieval of electron density from RO data. Some studies report errors between 10% and 20% for COSMIC-*Ne* compared to ground measurements of electron

density in the F-region (e.g., Pedatella et al., 2015; Yue et al., 2014). Liu et al. (2010) using OSSEs show that the errors in the RO-derived electron density could be as large as 100% in lower altitudes (below 200 km). These errors are mainly attributed to the assumption of spherical symmetry in the Abel inversion technique (see Liu et al., 2010; Pedatella et al., 2015, and references therein). Habarulema et al. (2014) show that different ionospheric parameters from RO-derived COSMIC and GRACE data correlate well with ionosonde measurements for 2008, which belongs to one of the periods investigated in this work. The COSMIC Data Analysis and Archive Center (website: <cosmic.ucar.edu>) disseminates the *level-2* post-processed GRACE and COSMIC electron density profiles used in this work. The supporting information includes an additional validation using in-situ electron density measurements from CHAllenging Minisatellite Payload (CHAMP; product identifier: CH-ME-2-PLPT).

The ensemble adjustment KF (EAKF)-based assimilation algorithm described in Anderson (2001) and implemented in the Data Assimilation Research Testbed-*classic* (DART; Anderson et al., 2009) is used to assimilate the data into TIE-GCM. Briefly, the EAKF is a deterministic method to compute the KF solution for a nonlinear forecast model (Anderson, 2001). The EAKF provides a relatively easy mechanism to assimilate observations into TIE-GCM to estimate the impact of the observations on the model state. Similar to the EnKF, EAKF uses sample statistics (means and covariances) from the prior ensemble of model states to calculate the posterior probability distributions. The probability distribution prior to the assimilation of data is referred to as the prior. The posterior is the probability distribution of the prior distribution updated with observations. Unlike the EnKF, the EAKF does not add noise from a sample of perturbed observations but applies the linear operator described in Anderson (2001) to update the prior ensemble of model states that yield theoretically consistent means and covariances. The EAKF uses the fifth order piecewise rational function described in Gaspari and Cohn (1999, Section 4c) to multiply the covariances between prior state vector and observations in order to constrain the spatial region of the impact of the observation on the model state. The text below refers to this parameter as the correlation function. Houtekamer and Mitchell (2001) provide a description of this spatial smoothing of the analysis increments in the context of atmospheric data assimilation, which is also the form adapted in the EAKF algorithm. The next section describes the specifics of the configuration and parameter settings used with the EAKF.

TIE-GCM is a well-established, physics-based, self-consistent model of the thermosphere-ionosphere system that uses a finite differencing technique to discretize the numerical solutions for the conservation of mass, energy, and momentum (e.g., Maute, 2017; Qian et al., 2014). TIE-GCM version 2.0 (released on 21 March 2016) with a model time-step of 30 s has been integrated into DART to perform the experiments presented here. The website www.hao.ucar.edu/modeling/tgcm provides more details about the open-source TIE-GCM code.

This study uses TIE-GCM with 5° × 5° and 0.5 scale-height resolutions in the horizontal (latitude and longitude) and vertical, respectively. The scale-height in the hydrostatic atmosphere assumed in TIE-GCM is the altitudinal difference as a result of change in air pressure by a factor of $1/e$, where e is the Euler's number (approximately 2.71828). In this configuration, TIE-GCM has 29 constant pressure surface layers that extend from approximately 97 to 600 km in altitude—the limit on upper boundary primarily depends on the level of solar activity. In the model runs presented here, the EUVAC (extreme ultraviolet flux model for aeronomic calculations) empirical solar proxy model (see Richards et al., 1994; Solomon & Qian, 2005) provides the solar irradiance input for TIE-GCM via the average of daily $F_{10.7}$ and its running 81-day centered mean $\bar{F}_{10.7}$. Heelis et al. (1982) ion convection model, and the Roble and Ridley (1987) auroral particle precipitation scheme specify the high latitude mean-energy, energy flux, and electric potential. Heelis et al. (1982) ion convection model uses the *Kp* index to estimate the hemisphere power and cross-polar-cap potential drop, which are required to determine the high latitude energy and momentum. The inbuilt wind dynamo calculates the electric potential for low and middle latitudes (see Richmond et al., 1992; Richmond, 1995). The Hagan et al. (2001) global scale wave model (GSWM) specifies the tidal forcing from the lower atmosphere through numerically derived migrating diurnal and semidiurnal tides at the lower boundary of TIE-GCM. This tidal forcing adds perturbations to, among others, the zonal mean values of neutral temperature and horizontal winds at the lower boundary, which are otherwise held fixed at 181 K and 0 m/s, respectively. The model runs presented here also adds day-of-year dependent perturbations to the advective and diffusive transport via the eddy diffusion coefficient as described in Qian et al. (2009).
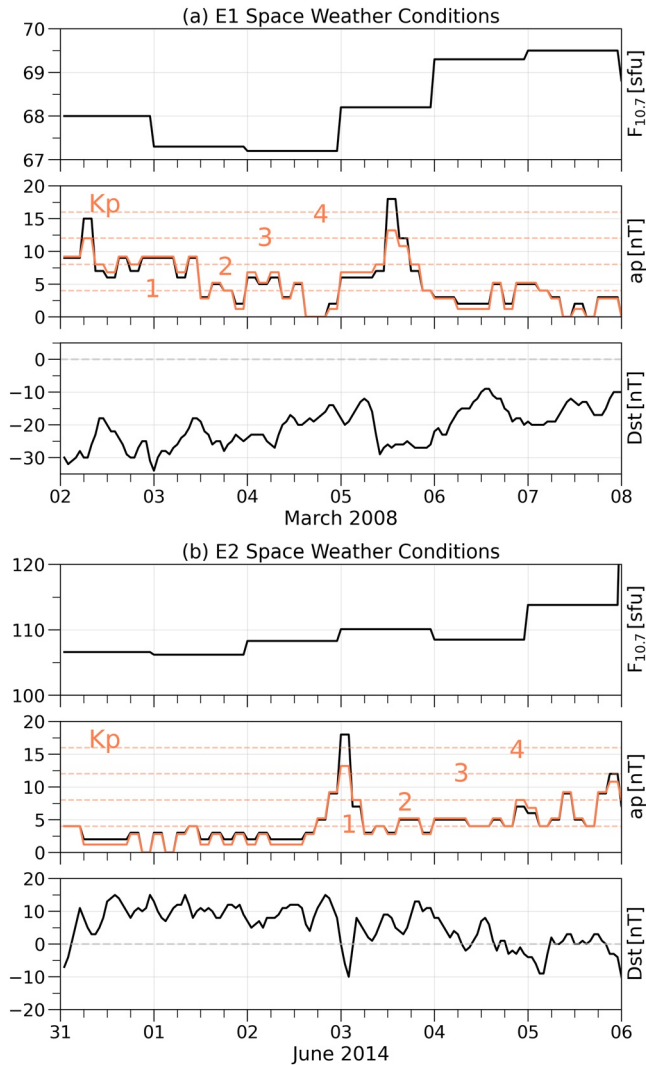
Figure 1. Space weather conditions for (a) March 2–8, 2008 and (b) May 31–June 6, 2014 demonstrated via $F_{10.7}$ solar flux, 3-h ap, and the Dst indices. The corresponding Kp values are overlaid on ap and marked in orange. Source: OMNI data available on omniweb.gsfc.nasa.gov.

3. Method

3.1. Data Assimilation Experiments

The following experiments are presented here to analyze the ability of the assimilation technique to guide TIE-GCM with realistic data:

E1 Assimilate COSMIC-Ne during solar minimum (4–8 March 2008); and

E2 Assimilate COSMIC-Ne during solar maximum (2–6 June 2014).

Assimilation of data during each period starts at 1 UT and ends at 0 UT on the respective days. The periods in 2008 and 2014 are selected to test the effectiveness of the assimilation during relatively low and high solar activity periods, respectively. The other criterion applied in selecting these periods is that they be relatively quiet (e.g., $Kp < 4$) in geomagnetic activity.

Figures 1a and 1b present the $F_{10.7}$ solar flux, 3-h ap, Kp, and Dst indices to illustrate the space weather conditions during E1 and E2, respectively. The geomagnetic activity indicated by ap, Kp, and Dst during both assimilation periods is largely quiet (e.g., $Kp < 4$). The solar activity during E2 (June 2014) is higher than that of E1 (March 2008) and appears to be steady with no large changes during both periods. The two periods provide an opportunity to compare the assimilation results at vastly different solar activity levels.

The assimilation window for both experiments E1 and E2 is 1 h. The spatial and local time coverage of COSMIC observations, as well as the number of observations in each assimilation window varies through the assimilation period and between experiments. The uncertainty of COSMIC observations is specified as a function of magnetic latitude, local time, and altitude based on Liu et al. (2010) and Yue et al. (2010). The supporting information provides the uncertainty percentages used in this study. Sections 3.2–3.5 provide other details pertinent to this study including assimilation control parameters, performance metrics, and limitations of the experiments.

3.2. Kalman Filter State Vector and Configuration of the Ensemble

The EAKF state vector $\boldsymbol{x}$ for the experiments in this work is composed of,

$$\boldsymbol{x} = [\boldsymbol{\psi}^{Tn}; \boldsymbol{\psi}^{\gamma O}; \boldsymbol{\psi}^{\gamma O^+}; \boldsymbol{\psi}^{\gamma O_2}; \boldsymbol{\psi}^{U}; \boldsymbol{\psi}^{V}; \boldsymbol{\psi}^{Ne}],$$

where Tn, O, O^+, O_2, U, V, and Ne represent the neutral temperature (K), atomic oxygen (γ [mass mixing ratio]), atomic oxygen ion (γ), molecular oxygen (γ), zonal (east-west) wind (m·s^{-1}), meridional (north-south) wind (m·s^{-1}), and electron number density (cm^{-3}), respectively. ψ denotes the full vector of the respective prognostic variable over the entire model space. Although the size of the assimilating observation vector may change in size with time, the size of $\boldsymbol{x}$ is constant. The mass mixing ratio γ of the major species is obtained with the assumption of $\gamma N_2 = 1 - (\gamma O + \gamma O_2 + \gamma He)$, thus affecting also the O/N$_2$ in $\boldsymbol{x}$. At the upper boundary of TIE-GCM, γO and γO_2 are in diffusive equilibrium. At the lower boundary of TIE-GCM, the vertical gradient of O is zero and the sum of mass mixing ratios of O and O_2 is 0.23 (Dickinson et al., 1984).

The thermosphere is driven by external heat and momentum sources, which are primarily characterized in TIE-GCM by the GPIs $F_{10.7}$ solar flux and Kp. The model error growth in EAKF is represented by the degree of spread among the ensemble of model states. If the GPIs are held constant then the probability distribution represented by the ensemble have no means of characterizing the effects of driver uncertainty

on the model error growth (Codrescu et al., 2018; Matsuo et al., 2013). Therefore, to aid the characterization of model error growth, the ensemble members for all experiments are generated by perturbing the primary forcing parameter $\boldsymbol{d}$ for each ensemble member m, where

$$\boldsymbol{d}^{(m)} = [F_{10.7}^{(m)}, \overline{F}_{10.7}^{(m)}, Kp^{(m)}].$$

$F_{10.7}, \overline{F}_{10.7}$, and Kp for $\boldsymbol{d}$ are sampled from a normal distribution as follows:

$$\boldsymbol{d}^{(m)} \hookleftarrow \mathcal{N}\left(\left[\mu_{F_{10.7}}, \mu_{\overline{F}_{10.7}}, \mu_{KP}\right], \ \left[\sigma^2_{F_{10.7}}, \sigma^2_{\overline{F}_{10.7}}, \sigma^2_{KP}\right]\right),$$

where μ is the mean and σ^2 is the variance of the respective distributions. The knowledge of the background GPIs for the respective periods in E1 and E2 determined the width of the $\boldsymbol{d}$ distributions. See Figure S1 for specific details of these distributions along with their respective statistics. The experiment assigns a nonrepeating combination of forcing parameters that makes up $\boldsymbol{d}$ to each ensemble member. This combination is fixed per m for the entire assimilation period.

3.3. Assimilation Parameters

The specifics of the DART configuration and parameter settings used here are as follows:

1. The ensemble size is 90 for each experiment;
2. The model error covariance is localized using the Gaspari and Cohn (1999) correlation function with a half-width of 0.2 radians horizontally;
3. The vertical localization height is 40 km;
4. The outlier threshold for observations is three SDs from the prior ensemble mean;
5. The assimilation window is 3600 s—centered at the current model time;
6. Spatially varying state space inflation is applied to the prior state before observations are assimilated with initial inflation, inflation SD, and inflation damping set equal to 1.02, 0.6, and 0.9, respectively;
7. The minimum Ne is 1000 cm^{-3};
8. The lower bound of the temperature is 100 K; and
9. The γO and γO_2 have cutoff limits at zero and one.

A 90-member ensemble is common among other similar experiments with DART/TIE-GCM as it provides a reasonable balance between computational load and ensemble spread (e.g., Lee et al., 2012; Matsuo et al., 2013; Hsu et al., 2014). The half-width value for the Gaspari and Cohn (1999) correlation function used in this study is similar to Matsuo et al. (2013) and Hsu et al. (2014). Chartier et al. (2016) considering the effect on total electron content (TEC) over the continental USA showed no appreciable difference between the use of localization half-width radii 0.2, 0.5, and 1.0 radians under geomagnetically quiet times. While Chartier et al. (2016) and Hsu et al. (2014) used no vertical localization, Matsuo et al. (2013) used a vertical localization height of 200 km in their experiment with synthetic data. In this context, the sensitivity of the different vertical localization heights is yet to be studied. The experiments in this study discard COSMIC-Ne values less than 1000 cm^{-3} and any value outside the abovementioned outlier threshold during the assimilation. The abovementioned spatially varying state space inflation values are thus specified on an ad-hoc basis following the recommendation in DART documentation for large geophysical models.

3.4. Model Runs and Evaluation Metrics

This study uses two states from each of the assimilation experiments: analysis $\boldsymbol{x}^a$ and forecast $\boldsymbol{x}^f$. The mean of the updated/posterior ensemble is referred to as the analysis state and the mean of the prior ensemble is referred to as the forecast state. The study assesses the assimilation results using these analyses and forecast states. As the assimilation window is centered at the current model time, it includes observations between ±30 min. Each forecast cycle projects the model forward by 1 h, and thus we refer to these forecasts as 1 h forecasts following the typical nomenclature (e.g., Chartier et al., 2016). The forecast run has no prior observations influencing the ensemble at the beginning of the experiment. However, the analysis run at

the beginning of the experiment (e.g., 1 UT on 4 March 2008 for E1) is updated with observations within the assimilation window. As the assimilation progresses, the forecast run uses the analysis state from the previous assimilation cycle to compute the expected state at the current assimilation cycle. For example, the forecast state at 2 UT used the analysis state at 1 UT as the initial conditions to drive the model forward by 1 h. In other words, the experiments do not assess the persistence of individual forecasts longer than 1 h.

The study also compares the results from the experiments with two other nonassimilation model runs: TIE-GCM control x^c and Evaluation-No Assimilation (hereinafter Eval-NA) x^{NA}. The observed GPIs for the respective periods in E1 and E2 are used to drive TIE-GCM to obtain the control state, which is sometimes referred to as GPI-driven TIE-GCM in the text. The initial conditions and background external forcing of Eval-NA runs are identical to that of the assimilation runs and reveals the direct impact of the assimilation of data relative to the background model. In short, Eval-NA is similar to analysis but without assimilation. All model runs including the TIE-GCM control and ensemble members are primed with a "spin-up" period of 15 days.

This study employs the following metrics to accomplish its objectives: root-mean-square error (RMSE), Pearson correlation coefficient, SD, model bias, percentage deviation of one distribution from another, and logarithm ratio of neutral mass density. The RMSE is computed as,

$$\text{RMSE} = \sqrt{\frac{1}{N}\sum_{i=1}^{N}\left(\text{Obs}_i - \text{Mod}_i\right)^2},$$ (1)

where N is the total number of observations, and Obs and Mod denote the observation and model estimate of the prognostic/diagnostic variable (e.g., Ne), respectively. The study defines model bias B as follows:

$$\text{B} = \text{Mod} - \text{Obs}.$$ (2)

In the following sections, Mod in Equations 1 and 2 is represented by either x^c, x^a, x^f, or x^{NA} as applicable.

The GPI-driven TIE-GCM control run is arguably the best estimate of the model without data assimilation. Therefore, the study uses the percentage change in RMSE of assimilation runs relative to the RMSE of TIE-GCM control run as a metric to indicate the benefit of data assimilation. Here, the percentage change in RMSE is defined as follows:

$$\frac{x_{\text{RMSE}} - x^c_{\text{RMSE}}}{x^c_{\text{RMSE}}} \cdot 100,$$

where x^c_{RMSE} is the RMSE of TIE-GCM control run and x_{RMSE} is replaced by the RMSE from either analysis or forecast as applicable. The study also uses the difference between the standard deviations of model estimates and COSMIC data ($|\sigma_M - \sigma_C|$) as a metric to indicate the impact of the assimilation in adjusting the model variability. Here, σ_M is represented by the SD of either TIE-GCM control run, analysis, or forecast as applicable. In these model-data comparisons, the model estimate is linearly interpolated to the observation location, first along the latitude and longitude and then to the altitude.

As per Emmert and Picone (2010), the study evaluates the changes to the neutral mass density ρ in the natural logarithm (ln) space. The logarithm ratio $\ln\left(\dfrac{x_\rho^{a,f}}{x_\rho^{NA}}\right)$ between the assimilation runs and nonassimilation run provides a direct measure of the scale of the impact of the assimilation of COSMIC-Ne on neutral mass density.

3.5. Limitations of the Experiments

This section highlights some limitations to consider with the results presented in this work. The assimilation scheme requires prior knowledge of the observation error variance. The imprecise and incomplete knowledge about the errors in the assimilating data (see Section 2) limits the accuracy of the observation
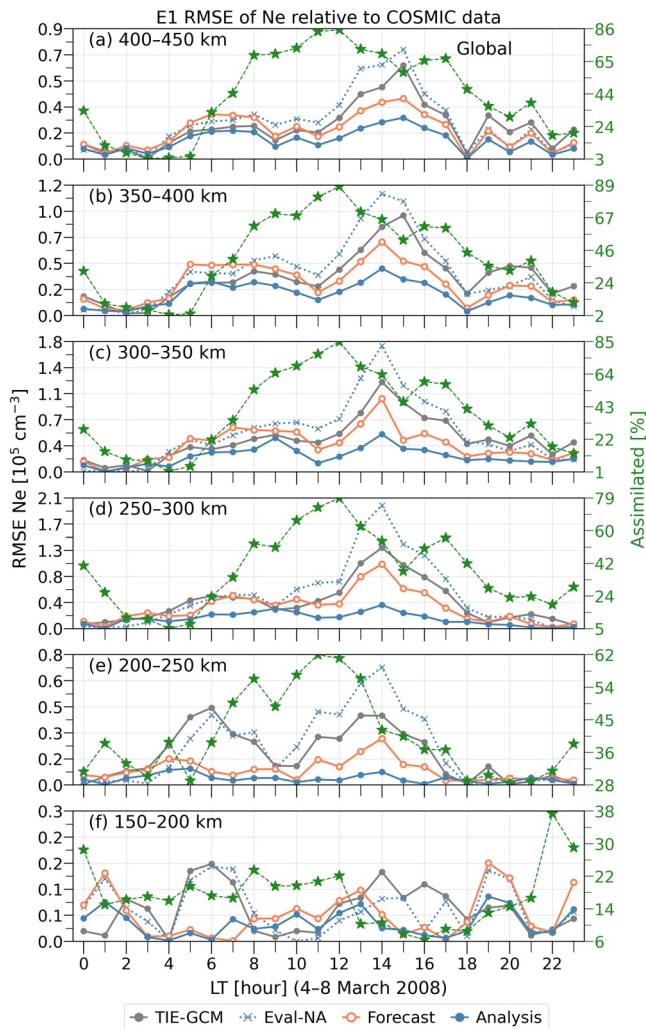
Figure 2. (a–f; left) The root mean square error (RMSE) of electron density (*Ne*) of the physics-based model TIE-GCM (gray), Eval-NA (Evaluation-No Assimilation; blue-dotted), forecast (orange), and analysis (blue) relative to COSMIC-*Ne* in the specified altitude region for the experiment E1. The results are grouped by local time of COSMIC data and represent the global mean. (a–f; right) The percentage of assimilated over total COSMIC-*Ne* observations in each LT-hour bin (green). The vertical scales are different in each panel. See Figures S2–S4 for results separated into different latitude regions.

error variance. The experiments use data that may not be available in near real-time, and thus the experiments are not entirely reflective of the performance of a true operational forecasting system.

Another limitation of the experiments is due to spurious correlations. The state vector x for the EAKF may generate spurious strong correlations between observations and model variables (e.g., winds, temperature, and composition). Spurious correlations occur, for example, as a result of long spatial distances between observation and model variable—spatially remote observations, and due to certain model variables being physically unrelated to the observation (Anderson, 2001). Spurious correlations between observations and physically unrelated model variables may be generated from limitations of the ensemble size, which is much less than the size of the state vector (Anderson, 2001). The size of the observation vector in the two experiments is also much smaller than the size of the state vector—an underdetermined system.

The correlation function partly addresses the problem of spurious correlations due to remote observations. In the experiments presented here, the correlation function shifts the impact of the observation from a maximum at the observation location to zero at a specified cutoff distance following an approximation of a Gaussian curve. A subset of TIE-GCM prognostic variables/fields is handpicked to address the problem of spurious correlations between observations and physically unrelated variables. The selected variables, which are known to be strongly correlated with mutual physical relationships forms the EAKF state vector. The assimilation scheme updates x per these correlations in each assimilation cycle. Lee et al. (2012), Matsuo et al. (2013), Hsu et al. (2014), and Chartier et al. (2016) presented results from different combinations of prognostic variables in the state vector. Overall, they demonstrated that inferring the dynamical state of both ionosphere and thermosphere is improved by including thermosphere-ionosphere coupling parameters such as electron density, temperature, winds, and composition in the state vector. The EAKF state vector x selected for this study is analogous to the superior-performing state vector in Hsu et al. (2014).

The geometric height in TIE-GCM is calculated using an empirical formulation relating spatially varying gravity with temperature and composition (Qian et al., 2014). This study interpolates model estimates to observation locations contingent on this geometric height. As the native vertical coordinate system in TIE-GCM is based on atmospheric pressure, a similar height conversion is done when assimilating COSMIC-*Ne* profiles into the model as COSMIC-*Ne* profiles do not include measured atmospheric pressure. These height uncertainties are further accentuated at higher altitudes as the conversion to geometric height expands the vertical resolution at higher altitudes between consecutive pressure layers. In other words, near the lower boundary, pressure levels converted to geometric height have a resolution of about 3 km, but pressure levels around 300-km altitude typically have a resolution greater than 30 km. The uncertainties introduced by this back-and-forth height conversion require further investigation.

4. COSMIC-Guided Ionosphere During Solar Minimum and Solar Maximum

4.1. Impact of the Assimilation by Local Time

Figure 2 shows the RMSE for E1 relative to COSMIC-*Ne* observations at six different altitude regions with a width of 50 km extending from 150 to 450 km. Figure 2 gives the RMSE as a function of local time (LT)

for the global-mean of *Ne* in states $\boldsymbol{x}^c$ control run (TIE-GCM; gray), $\boldsymbol{x}^{NA}$ (Eval-NA; blue-dotted), $\boldsymbol{x}^f$ (Forecast; orange), and $\boldsymbol{x}^a$ (Analysis; blue) at the assimilated COSMIC-*Ne* locations in the specified altitude region—computed as per Equation 1. The number of data points averaged in each altitude region per hour is not uniform and varies in local time. The right hand side ordinate gives the percentage of assimilated COSMIC-*Ne* observations out of the total available COSMIC-*Ne* observations (green). The results in Figure 2 thus only provide a relative indication of the impact of the assimilation. In other words, the RMSE shown in Figure 2 does not represent the globally averaged values across all local times with equal weight. As mentioned above, $\boldsymbol{x}^f$ is a 1-h forecast. Therefore, the forecast run has no prior observations influencing the ensemble at 1 UT on 4 March 2008. However, the analysis run at 1 UT on 4 March 2008 is updated with observations within the assimilation window. As the assimilation progresses, the forecast run uses the analysis state from the previous assimilation cycle to compute the expected state of the current assimilation cycle. For example, the forecast state at 2 UT used the analysis state at 1 UT as the initial conditions to drive the model forward by 1 h.

Several notable features of the evolution of the RMSE are present in Figure 2. As expected, the analysis state is mostly closer to COSMIC-*Ne* compared to the rest of the model runs across all six-altitude regions as indicated by the low RMSE values for the analysis run in Figure 2. This indicates the capability of the assimilation scheme to significantly impact the model state through assimilation of COSMIC-*Ne*. Figure 2 shows that the RMSEs for E1-analysis run, in general, are significantly lower than that of both TIE-GCM and Eval-NA during the daytime (06–18:00) in altitudes above 200 km.

Figure 2 indicates two RMSE-peaks for TIE-GCM: one around 6–8:00 and the other around 14:00. The largest RMSE values for both TIE-GCM and Eval-NA in multiple altitude regions in Figure 2 occur at 14:00. The RMSE-peaks for both TIE-GCM and Eval-NA at 14:00 are significantly higher than the respective peaks in the morning in altitudes above 250 km. The peak RMSEs for TIE-GCM, Eval-NA, and forecast in altitudes above 250 km are more than twice that of in altitudes below 250 km. Although the second peak around 14:00 is more pronounced for TIE-GCM, Eval-NA, and forecast in altitudes above 250 km, this signature of an increased RMSE around 14:00 is also clear for the analysis run. This RMSE-peak signifies a persistent model error against COSMIC data at this local time.

Figures 2a–2e show that the difference between Eval-NA and analysis is significantly larger during the daytime compared to that of night-time in altitudes above 200 km. The RMSE statistics here could be skewed due to the lack of assimilated observations during the nighttime compared to the daytime. Figure 2 indicates that the impact of the E1 assimilation is greater during the daytime in altitudes above 200 km. In general, the RMSEs for the forecast and analysis nearly follow each other except approximately between 12:00 and 15:00 in the 200–350-km altitude range (Figures 2c–2e). This indicates that in addition to the impact of the assimilation being greater in altitudes above 200 km for E1, the other forcing in the self-consistent model affecting the forecast step—leading to an increase in data-model bias, is also significant in these altitudes (which includes the ionosphere F-region). In other words, the forecast tend to evolve more toward the background model during 12–15:00 in the 200–350-km altitude range than at other times.

TIE-GCM's RMSE-peak at 6:00 is mostly suppressed in the forecast and analysis in the 200–250-km altitude range in Figure 2e. The number of COSMIC observations in this LT-hour bin is about 230. In higher altitudes (Figures 2a–2d), the number of assimilated COSMIC observations at 6:00 is less than that of in Figure 2e, and interestingly, the difference between TIE-GCM and the assimilation runs is also less than that of in Figure 2e. Figure 2 does not suggest a visible direct correlation between the number of assimilated observations and model performance but rather a local time dependent complex relationship between the two. Figure 2 suggests that more data are assimilated during the daytime compared to the nighttime (18:00–6:00). Figure 2 reveals that the *Ne* estimates from TIE-GCM with no help from data assimilation seem to agree well with COSMIC data during 18:00–4:00. Figure 2 also shows that, in general, the forecast and analysis are improved relative to both TIE-GCM control run and Eval-NA.

The presentation in Figure 3 is similar to Figure 2 except for E2, which focuses on the impact of assimilating COSMIC-*Ne* during solar maximum (2–6 June 2014). As expected, the analysis state is closer to COSMIC-*Ne* compared to the Eval-NA, forecast, and TIE-GCM across all six-altitude regions specified in Figure 3. Figure 3 shows that the E2-analysis run, in general, have significantly lower RMSE values than
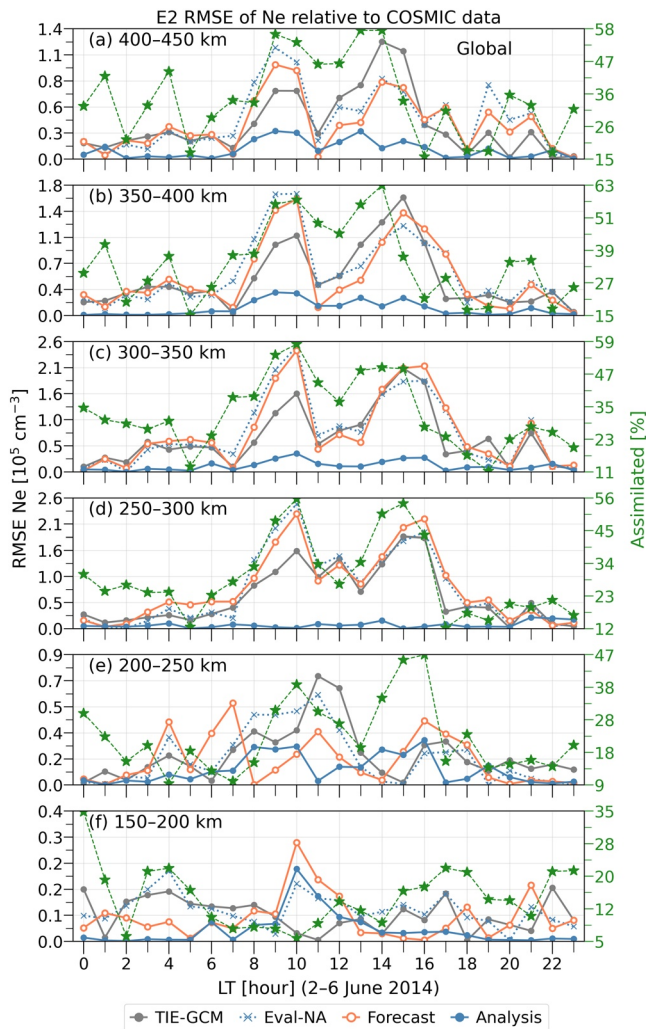
Figure 3. Same as Figure 2 except for E2.

that of TIE-GCM. Figure 3 also shows that the forecast run is not significantly different from both Eval-NA and TIE-GCM.

Figure 3 shows two prominent RMSE-peaks each for TIE-GCM, Eval-NA, and forecast around 10:00 and 15:00 LT in altitudes above 250 km. Such a local time dependent peak in RMSE is visible for the analysis run but not as significant as for the rest of the model runs. The forecast in the 250–450-km altitude range (Figures 3a–3d) is similar to Eval-NA, and their peak RMSE values are generally higher than that of TIE-GCM except in the 400–450-km altitude range.

TIE-GCM has a single pronounced RMSE-peak between 10:00 and 12:00 at the 200–250-km altitude range in Figure 3e, which is significantly higher than the highest RMSE for analysis and forecast in this altitude range. The forecast shows three prominent spikes in RMSE in Figure 3e. Both analysis and forecast share a pronounced RMSE-peak at 10:00 at the 150–200-km altitude range in Figure 3f. This may be due to the significant drop in the number of data points at 10:00. The range of RMSEs for the forecast, however, in the lower altitudes in Figures 3e and 3f is considerably lower than that in the higher altitudes. In Figure 3, TIE-GCM, Eval-NA, and forecast generally has lower RMSEs during nighttime compared to daytime but appears to be clearly separated from the analysis. A persistent minor peak in RMSE is apparent for TIE-GCM, Eval-NA, and forecast between 21:00 and 22:00 in altitudes above 250 km.

The E2-forecast in Figure 3 is not significantly different from that of Eval-NA in the 250–450-km altitude range. Figure 3 suggests that the impact of the assimilation on E2-forecast is marginal during daytime despite the relatively large number of observations assimilated during daytime. Although the number of assimilated observations per LT-hour is comparable between E1 and E2 (assimilated percentage marked in green in Figures 2 and 3), the number of assimilated observations is slightly higher for E2 (E1) in altitudes above (below) 250 km. The number of assimilated COSMIC profiles varies significantly also by latitude. Therefore, for completeness, Figures S2–S7 provide similar comparisons for different latitude regions. The main differences between the assimilation runs (both forecast and analysis), and Eval-NA and TIE-GCM that are present in Figures 2 and 3 are, in general, similar in different latitude regions (see Figures S2–S7), but these will be discussed in detail later.

4.2. Impact of the Assimilation by Altitude and Latitude

The comparison in Figure 4 supports Figures 2 and 3, and provides a more holistic view of the results from E1 (left column) and E2 (right column). The legend provided in Figure 4a applies also to panel 4d. Figures 4a and 4d show the vertical profiles of globally averaged electron density (COSMIC observations: green, Analysis: blue, Forecast: orange, TIE-GCM: gray) at the daytime sector defined here as between 06:00 and 18:00 LT. The resolution of the vertical profiles is 10 km, which corresponds to the vertical resolution of COSMIC data used in the assimilation. Figures 4a and 4d show that the assimilation of COSMIC-*Ne* seem to have a considerable impact on the model in altitudes above 250 km. The lack of impact below 250 km may be due to the large error specification at these altitudes, which could perhaps be mitigated by assimilating the raw slant TEC along the RO ray path. The E1- and E2-analysis runs are clearly separated from both the forecast and TIE-GCM, and is closer to the COSMIC-*Ne* profile in these altitudes above 250 km. In the peak electron density region, the E1-forecast is closer to COSMIC observations compared to TIE-GCM in Figure 4a. In Figure 4b, the E2-forecast is the furthest from COSMIC observations in the 250–350-km altitude range. In Figure 4a, the analysis run has corrected the height of the maximum electron density in addition to adjusting the magnitude of the electron density.
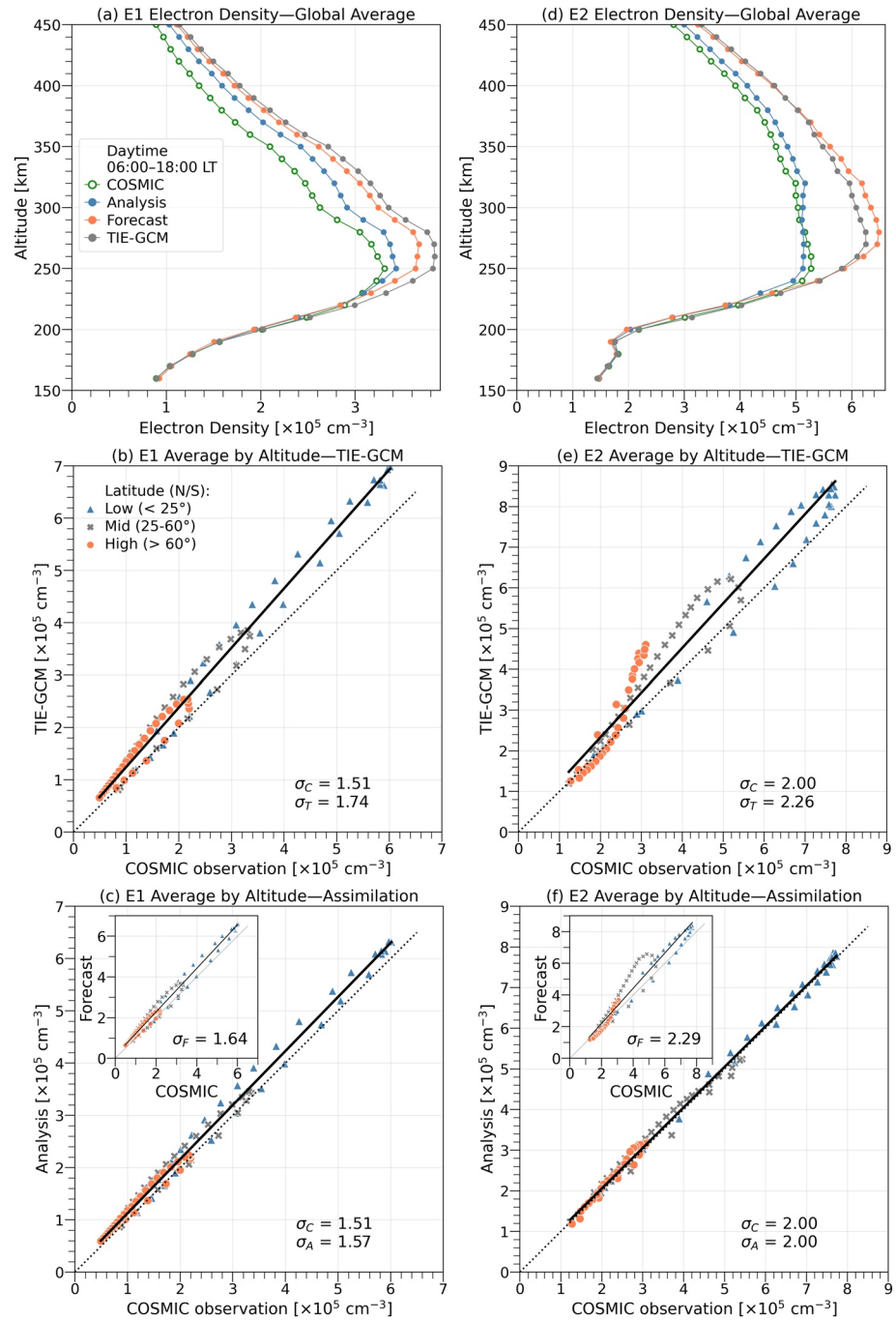
Figure 4. Vertical profiles of electron densities corresponding to the daytime sector in experiments (a) E1 and (d) E2. (b, c, e, and f) Statistical summary of the electron densities averaged in 10 km-altitude bins for (left) E1 and (right) E2. The geographic latitude regions are defined similar to Figure 8 σ_C, σ_T, σ_A, and σ_F refer to the SDs (in units of 10^5 cm^{-3}) of COSMIC, TIE-GCM, analysis, and forecast, respectively, considering the collective distribution across all latitudes. (c and f) The unit of COSMIC and forecast in the inset is 10^5 cm^{-3}. The scale and unit of the insets are identical to that of their corresponding main figure. The solid line is a linear fit considering the collective distribution, and the black dotted line represents the ideal data-model reference.

The legend provided in Figure 4b applies to the panels 4b,c,e, and 4f. Figures 4b–4c (4e–4f) provide a statistical summary of TIE-GCM, analysis, and forecast in E1 (E2) compared to COSMIC observations. The scale and unit of the inset—showing the results for the forecast, are identical to that of its corresponding main figure in Figures 4c and 4f. The results in Figures 4b, 4c, 4e, and 4f show the electron densities averaged per altitude-bin per latitude region (low: blue triangle, middle: gray cross, high: orange dot). The notations σ_C, σ_T, σ_A, and σ_F refer to the SDs (in units of 10^5 cm^{-3}) of COSMIC, TIE-GCM, analysis, and forecast, respectively, considering the collective distribution across all altitude-bins (global distribution).

The comparison in Figures 4b–4c clearly demonstrates that the assimilation of COSMIC-*Ne* in E1 has adjusted the range of the spread of electron densities in all three latitude regions—more significantly in the analysis than in the forecast. TIE-GCM in E1, in general, overestimates electron densities. In Figure 4e, TIE-GCM appears to significantly overestimate electron densities in some parts of the high latitudes and slightly underestimate in other parts of the high latitudes—orange dots above and below the dotted line. This overestimation is reduced in Figure 4f for both analysis and the forecast. Although the analysis has also adjusted the distribution well in middle and low latitudes in Figure 4f, the forecast does not show much difference in the middle latitudes and shows only a slight change in the low latitudes compared to TIE-GCM in Figure 4e. Considering the difference between the standard deviations of model estimates and COSMIC data, $|\sigma_F - \sigma_C|$ is smaller than $|\sigma_T - \sigma_C|$ for E1 compared to that of E2—the difference between σ_F and σ_T in E2 is, however, marginal. σ_A in both E1 and E2 are similar to σ_C. This is expected as σ_A is a function of σ_C and σ_F in the Bayes' theorem. This effort of the KF, in general, to minimize the mean square error of the estimated quantity is visible across all altitudes and latitude regions.

The presentation in Figure 5 is similar to Figure 4 except for night-time (18:00–06:00 LT). Similar to Figure 4a, Figure 5a shows no significant impact of the assimilation in altitudes below approximately 250 km—the scale of the electron density in the two figures are different. The analysis run is clearly separated from both the forecast and TIE-GCM, and is closer to the COSMIC-*Ne* profile in altitudes above 270 km in Figure 5a. The forecast begins to separate from TIE-GCM and move closer to the COSMIC-*Ne* profile in altitudes above approximately 300 km. Thus, in the nighttime peak electron density region the assimilation runs are clearly separated from TIE-GCM in E1.

E2-forecast for nighttime electron densities in Figure 5d is not significantly different from that of TIE-GCM. TIE-GCM control run underestimates electron density for the most part of the profile shown in Figure 5d—in contrast to TIE-GCM's trend in daytime for E1 and E2, and nighttime for E1. This may indicate the enhancement in summer nighttime electron density in data. The E2-analysis is in excellent agreement with nighttime COSMIC-*Ne* profile.

Similar to daytime E1 in Figures 4, Figures 5b–5c demonstrate that the assimilation of COSMIC-*Ne* has significantly adjusted the range of the spread of nighttime electron densities. The σ differences between the E2 assimilation runs and TIE-GCM control run in Figures 5e–5f are not as large as they are for E1. Figures 5e and 5f indicate that the E2-forecast underestimate electron densities in the high latitudes slightly more than TIE-GCM.

Table 1 summarizes key statistics of the two experiments. Table 1 provides the Pearson correlation coefficient Pr, the difference between the standard deviations of model estimates and COSMIC data ($|\sigma_M - \sigma_C|$; see Section 3.4), and the RMSE for different altitude regions. The quantity $|\sigma_M - \sigma_C|$ for the analysis and forecast indicates the impact of the assimilation in adjusting the spread of their respective electron density distributions. A smaller difference in $|\sigma_M - \sigma_C|$ indicates that the variability of the electron density estimates of the model is closer to that of COSMIC data. Table 1 also provides the SD of COSMIC data σ_C along with the percentage of the assimilated data out of the total available COSMIC-*Ne* observations for each of the six-altitude regions used in Figure 2.

Table 1 shows that the assimilation scheme used in this study rejects a large portion of the COSMIC data in both E1 and E2 in the 150–200-km altitude range. This large rejection could be due to small model spread at these altitudes (see outlier threshold in Section 3.3). In the next altitude region (200–250 km), the percentage of assimilated data is significantly higher (41%) for E1 under solar minimum conditions but remains low (23%) for E2 under solar maximum conditions. In other altitude regions (250–450 km), this percentage of assimilated data is comparable but the overall rejection ratio during E2 is higher than that
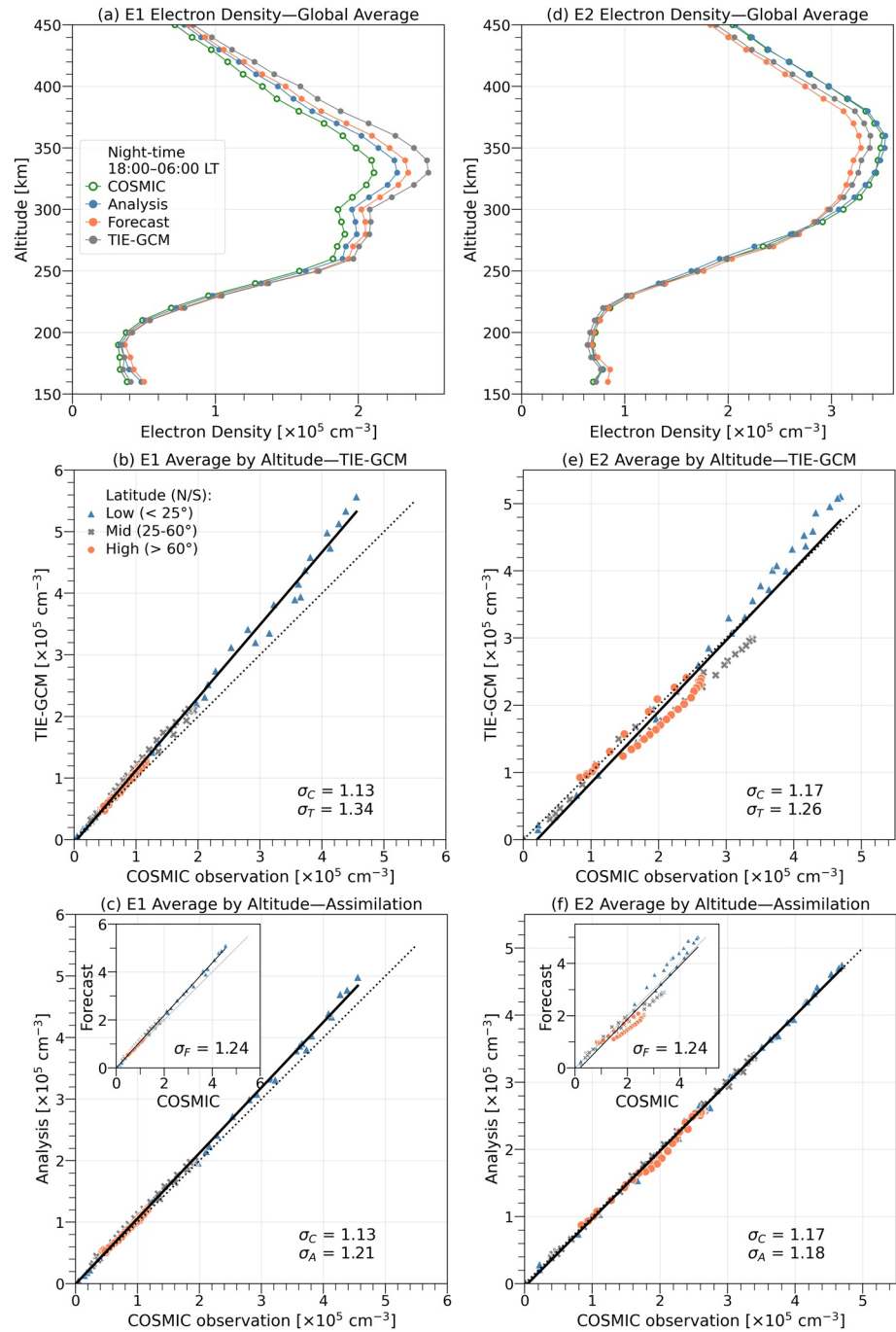
Figure 5. Same as Figure 4 except for nighttime.

of E1. $|\sigma_M - \sigma_C|$ clearly separates the results in Table 1 into two altitude groups: above and below 250 km. The $|\sigma_M - \sigma_C|$ values for analysis and forecast are significantly lower for altitudes above 250 km compared to that of altitudes below 250 km. The Pearson correlation coefficients for TIE-GCM control run and the assimilation runs are comparable with each other in each altitude region. In general, the Pr is marginally stronger for the TIE-GCM control run in E1 and analysis in E2.

Figure 6 shows the geographic latitude and altitude distribution of the model bias (see Equation 2) relative to COSMIC-*Ne* for E1. Figure 6 also shows the variation of the height of maximum *Ne* in each latitude column for COSMIC (solid line) and respective model (dotted line). Here the height of maximum *Ne* is not

Table 1
Low-Order Statistics of the Data Assimilation Experiments

	E1 (solar minimum)			E2 (solar maximum)		
	TIE-GCM	Analysis	Forecast	TIE-GCM	Analysis	Forecast
150–200 km	$\sigma_C = 1.27; A = 15.13\%$			$\sigma_C = 1.55; A = 13.52\%$		
Pr	0.77	**0.80**	**0.80**	0.77	**0.78**	0.77
$\lvert\sigma_M - \sigma_C\rvert$	**0.51**	0.52	0.53	**0.55**	0.58	0.59
RMSE	0.07	**0.04**	0.06	0.08	**0.04**	0.07
200–250 km	$\sigma_C = 2.03; A = 41.00\%$			$\sigma_C = 2.45; A = 23.21\%$		
Pr	0.76	**0.77**	0.75	0.74	**0.77**	0.73
$\lvert\sigma_M - \sigma_C\rvert$	**0.50**	0.60	0.59	**0.57**	0.68	0.60
RMSE	0.19	**0.04**	0.09	0.21	**0.10**	0.17
250–300 km	$\sigma_C = 2.23; A = 39.09\%$			$\sigma_C = 2.70; A = 31.30\%$		
Pr	**0.78**	0.75	0.74	0.63	**0.65**	0.54
$\lvert\sigma_M - \sigma_C\rvert$	**0.03**	0.20	0.18	0.20	0.44	**0.18**
RMSE	0.42	**0.16**	0.34	0.64	**0.07**	0.81
300–350 km	$\sigma_C = 1.94; A = 41.36\%$			$\sigma_C = 2.88; A = 35.84\%$		
Pr	**0.85**	0.82	0.81	0.70	**0.72**	0.62
$\lvert\sigma_M - \sigma_C\rvert$	0.37	**0.14**	0.16	0.10	0.06	**0.02**
RMSE	0.45	**0.21**	0.37	0.68	**0.12**	0.80
350–400 km	$\sigma_C = 1.42; A = 44.62\%$			$\sigma_C = 2.66; A = 38.33\%$		
Pr	**0.88**	0.86	0.85	0.78	**0.80**	0.74
$\lvert\sigma_M - \sigma_C\rvert$	0.30	**0.10**	0.13	0.35	**0.14**	0.15
RMSE	0.35	**0.19**	0.30	0.51	**0.10**	0.53
400–450 km	$\sigma_C = 0.92; A = 47.63\%$			$\sigma_C = 2.11; A = 38.05\%$		
Pr	**0.88**	0.87	0.86	0.82	**0.83**	0.79
$\lvert\sigma_M - \sigma_C\rvert$	0.12	**0.01**	**0.01**	0.36	**0.12**	0.16
RMSE	0.22	**0.13**	0.19	0.37	**0.10**	0.37

Note: Pr is Pearson correlation coefficient between COSMIC-*Ne* data and the specified model. The unit of SD σ and root-mean-square error (RMSE) is 10^5 cm^{-3}. σ_C is for COSMIC-*Ne* data and σ_M is for either TIE-GCM, analysis, or forecast as applicable. A is the percentage of assimilated over total COSMIC-*Ne* observations in the specified altitude region. RMSE is relative to COSMIC data for the specified model in the specified altitude region. The values in bold emphasize the largest Pr and the smallest $\lvert\sigma_M - \sigma_C\rvert$ and RMSE for each category.

provided for any latitude column that has at least one latitude-altitude bin with no data. The resolution of the representation in Figure 6 is 5° in latitude and 10 km in altitude. The presentation in Figure 7 is similar to Figure 6 except for E2. The number of observations available per latitude-altitude bin varies. Figures S8 and S9 show the raw data used in the bias calculation along with the number of observations averaged per latitude-altitude bin for E1 and E2, respectively.

All four model representations in Figure 6 show good agreement with COSMIC-*Ne* in high southern latitudes as indicated by low model bias in latitudes south of approximately 45°S. Figures 6a and 6c show that both TIE-GCM and the nonassimilation run Eval-NA have a strong positive bias in latitudes north of 45°S and above approximately 200 km altitude. Figure 6b shows that the analysis run has significantly reduced the model bias across all latitudes. The forecast in Figure 6d also shows, in general, a significant reduction in the model bias compared to TIE-GCM and Eval-NA but a larger bias than the analysis especially pronounced in low to middle northern latitudes.

All four model representations of the height of maximum *Ne* show excellent agreement in latitudes between 30°S and 30°N. In comparison to the Eval-NA run in Figures 6c, Figure 6b shows that the analysis run has adjusted these heights to be more in line with that of COSMIC in middle to high latitudes. The heights of maximum *Ne* of the forecast in Figure 6d are not significantly different from that of Eval-NA. Interestingly, while the analysis has significantly reduced the height of maximum *Ne* from that of Eval-NA around 75°S, the forecast has moved this height further up.

Figure 7 shows a hemispheric asymmetry in TIE-GCM's model bias in altitudes above 200 km relative to COSMIC-*Ne*. In the northern summer hemisphere, TIE-GCM significantly underestimates electron density. While the analysis (Figure 7b) has significantly reduced the model bias across all latitudes, the forecast (Figure 7d) only shows some moderate improvement around the equator. Figure 7b also shows that the analysis has significantly adjusted the height of maximum *Ne* in high southern latitudes. In Figure 7b, the analysis seems to overestimate the height of maximum *Ne* in northern summer high latitudes while reducing TIE-GCM's systematic underestimation of electron density in the region. Similar to E1 in Figure 6, the heights of maximum *Ne* of the forecast in Figure 7d are not significantly different from that of Eval-NA.

Table 2 summarizes the percentage change in RMSEs of analysis and forecast for both E1 and E2. Section 3.4 describes how the percentage change in RMSE is calculated for Table 2. Such percentage changes in RMSEs reveal the performance of the assimilation runs compared to the TIE-GCM control run, which is not assisted with data assimilation for its electron density estimates. In Table 2, the negative (positive) values indicate the percentage by which the RMSE is reduced (increased) in the analysis or forecast compared to x^c_{RMSE}. Table 2 summarizes these results for the change in RMSEs by four different latitude categories and the six altitude regions used in Figures 2 and 3 considering the entire respective periods of E1 and E2. The results in Table 2 correspond to the mean values of the specified altitude-latitude region.

Table 2 highlights that E1 under solar minimum conditions reduces the RMSE of the analysis and forecast except for the forecast in high latitudes in the 150–200-km altitude range. As expected, the RMSE of the analysis is reduced much more significantly than that of the forecast. In general, the E1-forecast is
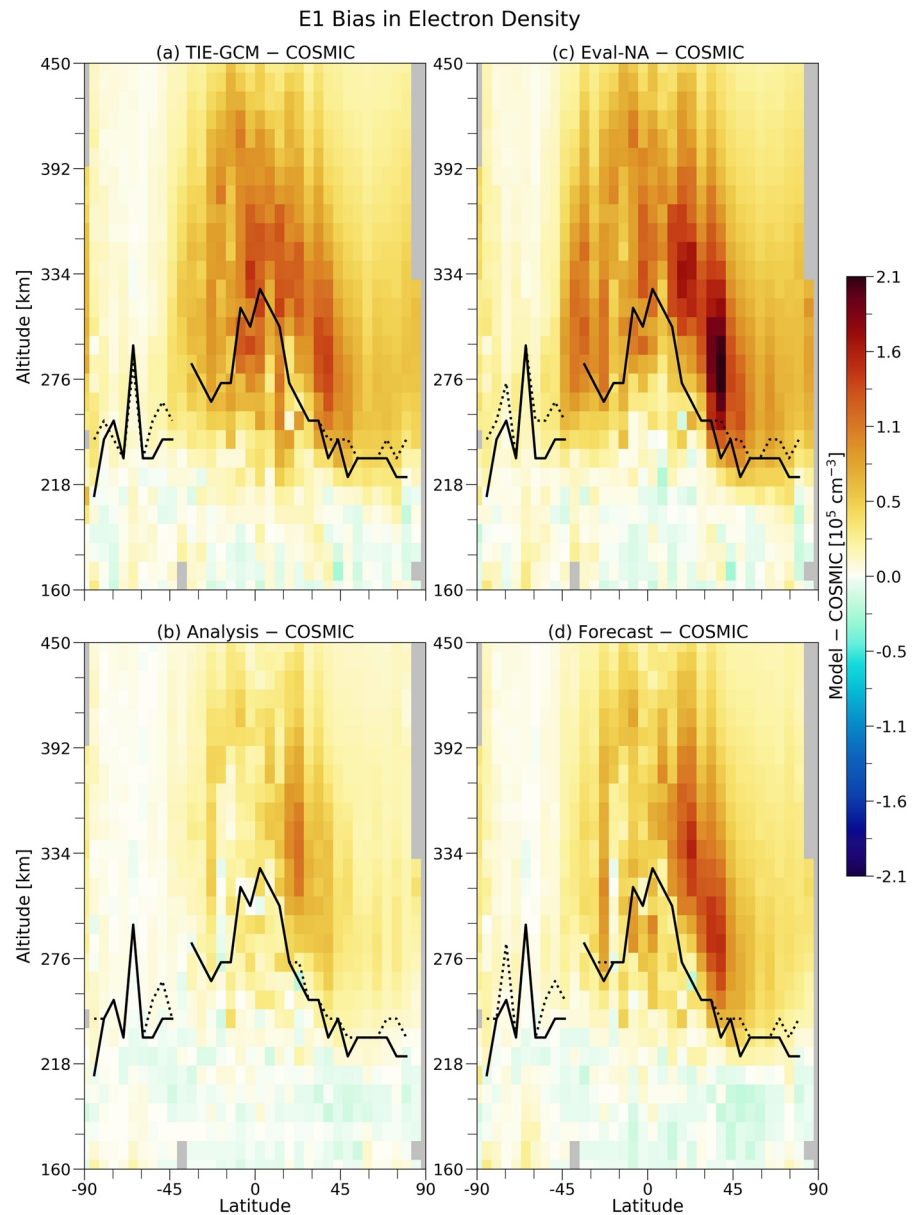
Figure 6. (a–d) The geographic latitude (positive = North; negative = South) and altitude distribution of the difference between model estimated electron density (*Ne*) and COSMIC-*Ne*. The black solid (dotted) line represents the height of maximum *Ne* for COSMIC (model) in each latitude column. The height of maximum *Ne* is not provided for any latitude column with at least one bin with no data (gray areas). The resolution of the data is 5° in latitude and 10 km in altitude. Figure S8 shows the corresponding raw data and the number of observations averaged per latitude-altitude bin.

significantly better in the low latitudes than in the middle latitudes. In altitudes above 200 km, the performance of E1-forecast is comparable in both high and low latitude regions. The results for E1 in Table 2 considering the global mean and individual latitude regions indicate that both analysis and forecast perform consistently well in the 200–250-km altitude range compared to other altitude regions. Table 2 reveals that the performance of the forecast significantly drops in the 250–450-km altitude range in middle latitudes, which is also the altitude-latitude region where the difference between the RMSEs of analysis and forecast is, in general, largest.

Table 2 highlights that the global performance of the E2-analysis is outstanding in the 250–450-km altitude range compared to that of E1—a difference of approximately 30%. E1-analysis outperforms the E2-analysis
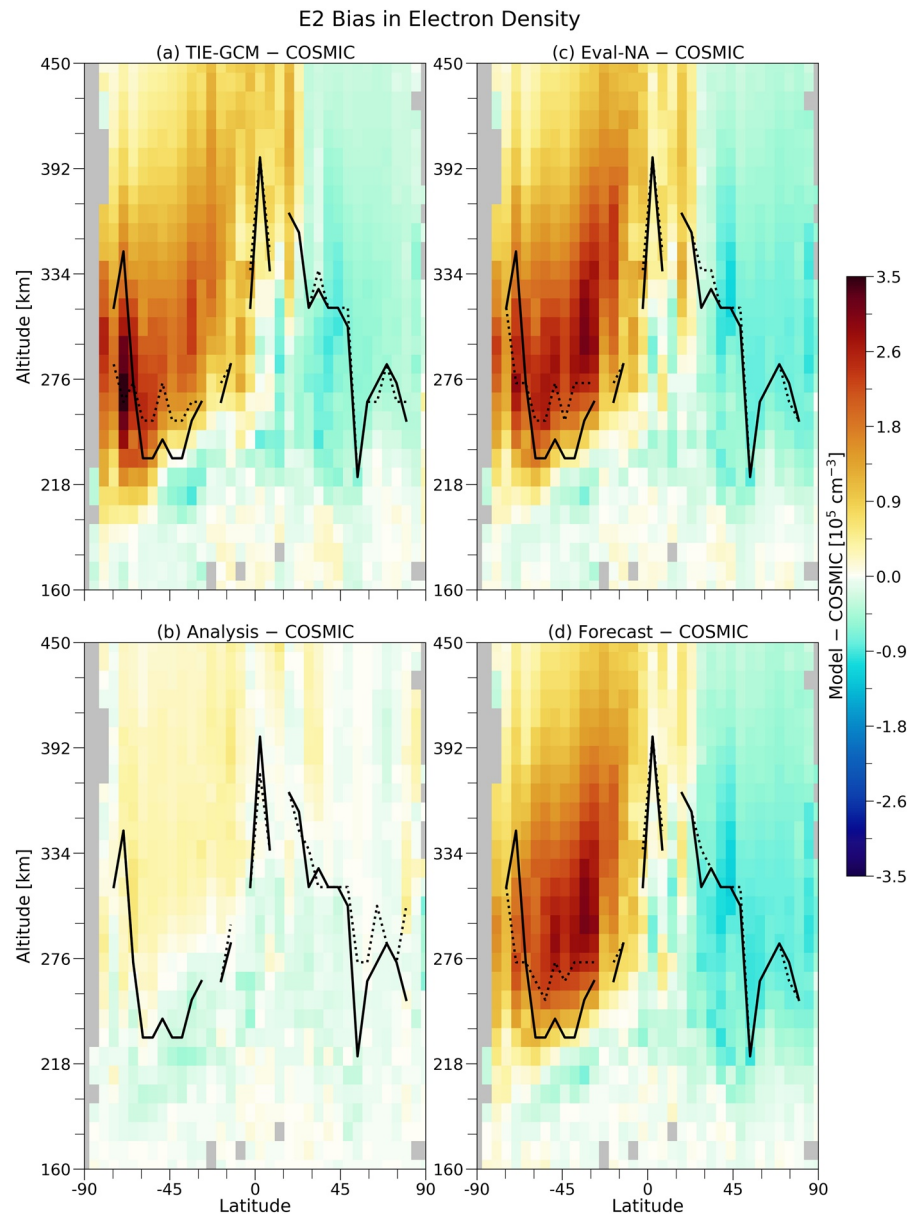
Figure 7. Same as Figure 6 except for E2. Figure S9 shows the corresponding raw data and the number of observations averaged per latitude-altitude bin.

in the 200–250-km altitude range, and it is clear from Table 2 that the poor performance of E2-analysis in this altitude range mostly occurs in the middle latitudes. A significant latitudinal dependency in performance is not apparent for the analysis in both E1 and E2.

The performance of the E1-forecast is significantly better than the E2-forecast, which is under solar maximum conditions. Table 2 reveals that the poor performance of E2-forecast in the 250–350-km altitude range in Figure 3 could mainly be attributed to its performance in the middle latitudes. Similarly, this poor performance in the 350–450-km altitude range could mainly be attributed to the performance in the high latitudes.

Table 2
Change in RMSEs of Analysis and Forecast From the RMSE of TIE-GCM

| Altitude region (km)	E1 (solar minimum)		E2 (solar maximum)	
	Analysis (%)	Forecast (%)	Analysis (%)	Forecast (%)
Global				
150–200	−42.86	−14.29	−50.00	−12.50
200–250	−78.95	−52.63	−52.38	−19.05
250–300	−61.90	−19.05	−89.06	**26.56**
300–350	−53.33	−17.78	−82.35	**17.65**
350–400	−45.71	−14.29	−80.39	**3.92**
400–450	−40.91	−13.64	−72.97	**0.00**
High Latitudes (60° − 90°N/S)				
150–200	−37.50	**12.50**	−42.86	**42.86**
200–250	−76.47	−52.94	−79.07	−37.21
250–300	−59.38	−34.38	−85.29	−21.57
300–350	−57.14	−25.00	−80.28	**1.41**
350–400	−52.63	−21.05	−63.16	**36.84**
400–450	−42.86	−14.29	−52.00	**52.00**
Middle Latitudes (25° − 60°N/S)				
150–200	−41.67	−8.33	−53.85	−30.77
200–250	−76.47	−47.06	−35.00	**0.00**
250–300	−60.98	−12.20	−89.33	**33.33**
300–350	−46.51	−4.65	−83.54	**24.05**
350–400	−43.75	−9.38	−78.57	**16.07**
400–450	−36.84	−5.26	−66.67	**6.06**
Low Latitudes (25°S − 25°N)				
150–200	−75.00	−50.00	−66.67	−55.56
200–250	−57.14	−46.43	−54.17	−29.17
250–300	−61.73	−40.74	−77.78	**2.22**
300–350	−55.14	−28.04	−77.42	**0.00**
350–400	−49.43	−26.44	−77.03	−6.76
400–450	−44.64	−17.86	−75.34	−8.22

Note: The negative (positive) values indicate the percentage by which the RMSE is reduced (increased) in the analysis or forecast compared to the RMSE of TIE-GCM control run computed against COSMIC-*Ne* as per Equation 1. The negative values indicate that the respective estimate of electron density is closer to COSMIC observations than TIE-GCM. The positive values in bold represent the regions where the data assimilation runs perform poorly compared to the TIE-GCM control run.

5. Forecasts of the Experiments

5.1. Sensitivity of the Forecasts to the Assimilation of COSMIC-*Ne*

The focus of this section is to investigate the forecasting capability of the assimilation scheme with COSMIC observations. Figure 8 provides a point-to-point direct comparison of E2 electron density estimates from TIE-GCM control (left column) and forecast (right column) runs with COSMIC observations at three altitude regions—here the TIE-GCM and forecast estimates are interpolated to the observation location. The legend provided in Figure 8e applies to all the panels 8a–8f. Figure 8 is a multidimensional scatter plot revealing other aspects of the compared electron density distributions. The data points in orange (1-h forecasts) indicate whether the particular COSMIC-*Ne* observation was assimilated in the next assimilation cycle to produce the analysis state. The COSMIC observations that were discarded by the assimilation scheme
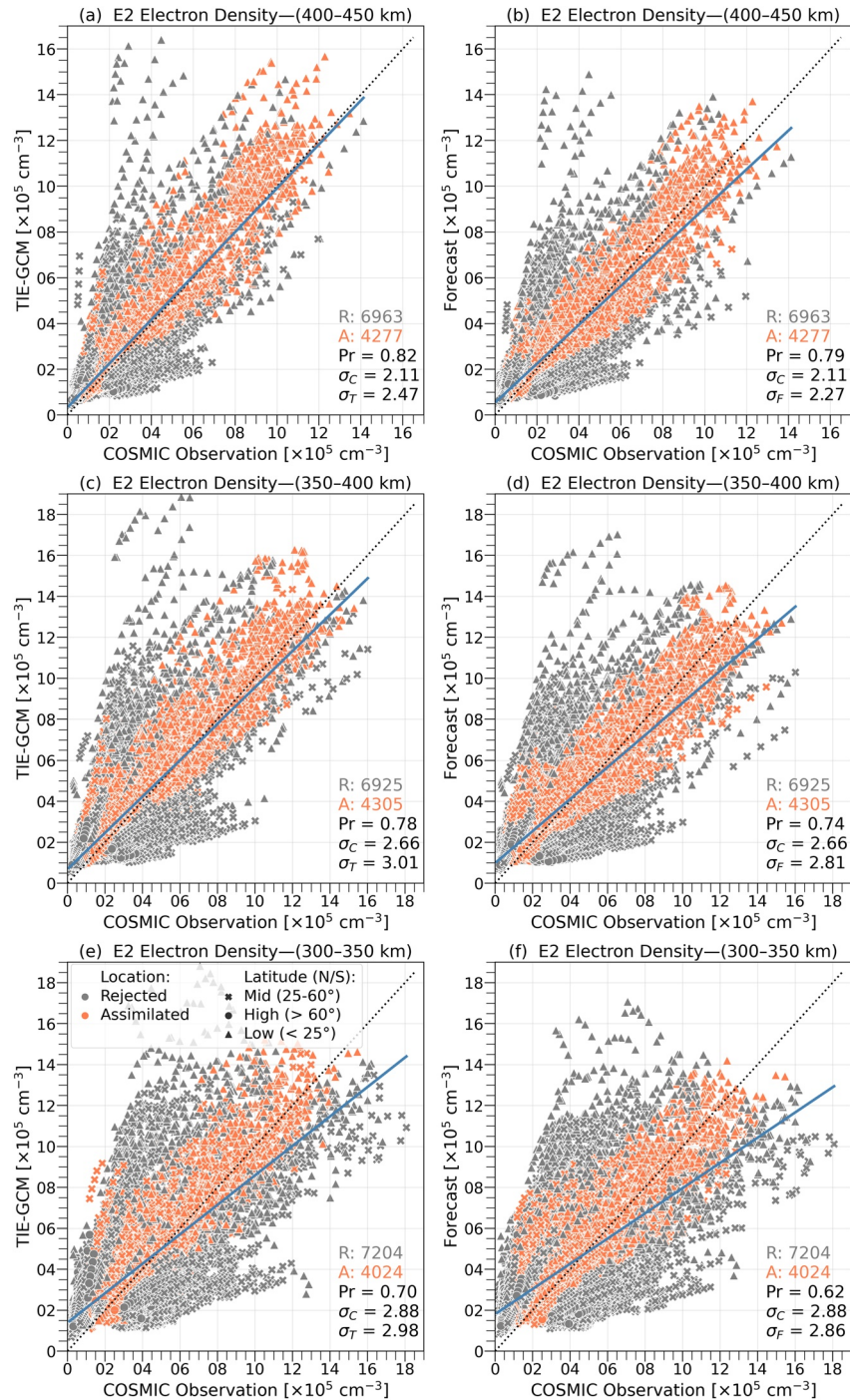
Figure 8. (a–f) A multidimensional scatter plot comparing electron density observations of COSMIC with that of (left column) TIE-GCM and (right column) forecast in E2 at the specified altitude region. The location of the data points are color-coded as follows: the data points in orange (gray) indicate whether the particular COSMIC observation was assimilated (rejected) in the next assimilation cycle to produce the analysis state. The forecast shown here is only influenced by COSMIC observations that were assimilated in previous assimilation cycles and not the particular observation that it is compared to in the current assimilation cycle. The total number of rejected (assimilated) observations in the distribution are noted as R (A). Pr is the Pearson correlation coefficient between distributions specified in the abscissa and ordinate. σ_C, σ_T, and σ_F give the standard deviations (in units of 10^5 cm^{-3}) of COSMIC, TIE-GCM, and forecast, respectively, considering the entire population in the specified altitude region. The geographic latitude of the observations are separated into three categories: low (25°S–25°N; triangle), middle (25°–60°N/S; cross), and high (60°–90°N/S; dot). The solid blue line is a linear fit considering all observations, and the black dotted line represents the ideal data-model reference.

in the update/analysis step are shown in gray. The forecast shown here is only influenced by COSMIC-*Ne* observations that were assimilated in previous assimilation cycles and not the particular observation that it is compared to in the current assimilation cycle. The total number of rejected (assimilated) observations in the distribution are noted as R (A) in each scatter plot. The notations Pr, σ_C, σ_T, and σ_F in Figure 8 give the Pearson correlation coefficient between distributions specified in the abscissa and ordinate, standard deviations (in units of 10^5 cm^{-3}) of COSMIC, TIE-GCM, and forecast, respectively, considering the entire population in the specified altitude region. The solid blue line is a linear fit considering all observations, and the black dotted line represents the ideal data-model reference. Figure 8 also indicates the geographic latitude of the observations in three categories: low (25°S–25°N; triangle), middle (25°–60°N/S; cross), and high (60°–90°N/S; dot). This visualization is aimed at recognizing parts of the distribution with characteristics unique to a certain latitude region, such as that most large electron densities in COSMIC data above 300 km altitude occur in the middle latitudes (see Figures 8c–8f). For completeness, Figures S10–S12 provide such comparisons for the lower altitude regions and E1.

Figure 8 illustrates the impact of the assimilation on the forecast distribution compared to the standalone GPI-driven TIE-GCM run. The difference between the SDs of COSMIC data and forecast distributions is less than that of the TIE-GCM control run ($|\sigma_F - \sigma_C| < |\sigma_T - \sigma_C|$). In other words, the variability of the electron density estimates of the TIE-GCM control run is higher than that of COSMIC data and E2-forecast in Figure 8. In Figure 8, the forecast estimates display a remarkable precision relative to COSMIC observations at the locations where data are assimilated in the next assimilation cycle (marked in orange). This is likely due to observations at or near these locations marked in orange but belonging to a previous assimilation cycle that have been assimilated, which allows the model to self-consistently evolve in response to the altered state. The information about the rejected observations are not passed into the model. A notable feature of Figure 8 is that, although the agreement between COSMIC data and forecast seems better at locations marked in orange, the Pearson correlation coefficient considering the whole distribution is slightly larger for the TIE-GCM control run.

Figure 8 demonstrates an underlying altitude-latitudinal structure in model-data agreement. Figure 8 indicates that severe overestimation (underestimation) of electron density in both TIE-GCM control run and forecast mostly occurs in low (middle) latitudes. On the one hand, TIE-GCM control run significantly overestimates electron density at certain low latitude observations (gray triangles on top-left in Figure 8a), and significantly underestimates at certain other low latitude observations (scattered gray triangles below the dotted line in Figure 8e). This disagreement between the overestimated electron densities in the low latitudes is considerably reduced in the forecast in Figure 8b. The underestimated low latitude densities in Figure 8e seems to have moved slightly closer to the ideal data-model reference line in Figure 8f. This indicates that E2-forecast has improved relative to COSMIC-*Ne* in the region as a whole and not just where the observations were assimilated. On the other hand, in Figure 8e, most of the underestimated electron densities belong to middle latitudes. The corresponding part of the distribution in Figure 8f is not changed much in the forecast. In general, Figure 8 illustrates that the assimilation has bent the forecast distribution toward the ideal data-model reference line. These characteristics of the distributions change significantly by altitude and latitude between the two experiments E1 and E2 as discussed in Table 1 and Figures 4 and 5 where the results from the two experiments are summarized.

### 5.2. COSMIC-Guided Forecasts Compared to GRACE Data

This section investigates the forecast states from the two experiments E1 and E2 with independent GRACE electron density data. The validation results in Figures 9 and 10 correspond to E1 and E2, respectively. Figures S13 and S14 provide an additional validation along the orbit of the CHAMP satellite.

The legend provided in Figure 9a applies to panels 9a–9d. The electron density profiles shown here (GRACE observations: green, Forecast: orange, TIE-GCM: gray) have a vertical resolution of 10 km and correspond to the local time sector 16:00–18:00 LT. As the GRACE orbit is quasi-Sun-synchronous, this local time sector provides more GRACE data than other times, and such selection reduces skewing of the profiles due to uneven time sampling. While Figure 9d shows the vertical profiles of electron density averaged across all latitudes, Figures 9a–9c correspond to low, middle, and high latitude regions, respectively.
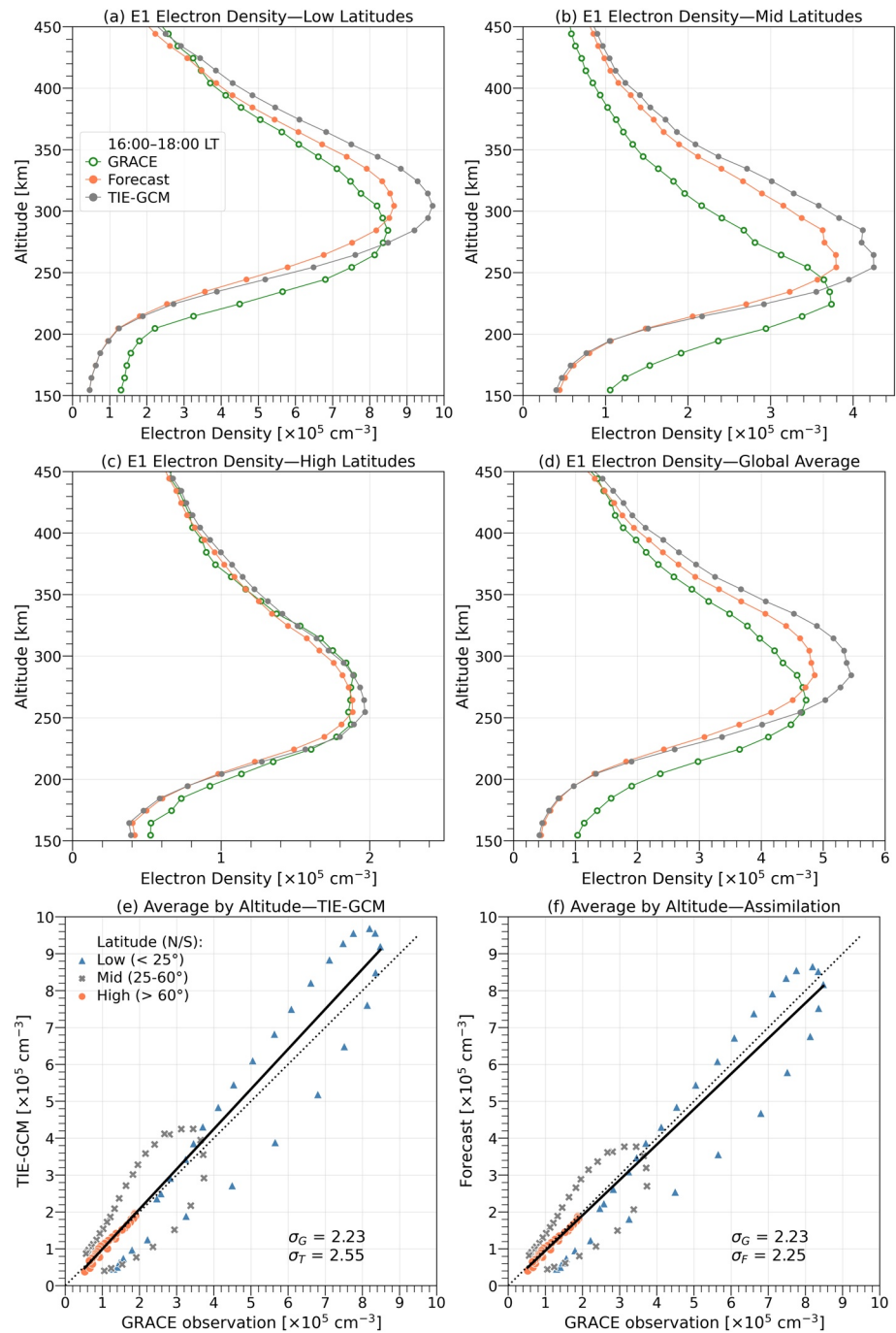
Figure 9. Results of E1 compared to independent GRACE data. (a–d) Vertical profiles of electron densities at the specified latitude region corresponding to the 16–18 local time sector. (e–f) Statistical summary of the electron densities averaged in 10 km-altitude bins. The geographic latitude regions are defined similar to Figure 8 σ_G, σ_T, and σ_F refer to the standard deviations (in units of 10^5 cm^{-3}) of GRACE, TIE-GCM, and forecast, respectively, considering the collective distribution across all bins. The solid line is a linear fit considering the collective distribution, and the black dotted line represents the ideal data-model reference.

In the low latitudes, in Figure 9a, the forecast is significantly different from TIE-GCM above the altitude of 250 km, and closer to the GRACE profile from approximately 280 to 420 km. In altitudes below 250 km, both TIE-GCM and forecast seem to significantly underestimate electron densities compared to GRACE data. In the middle latitudes, in Figure 9b, the forecast shows a shift toward GRACE data above the altitude
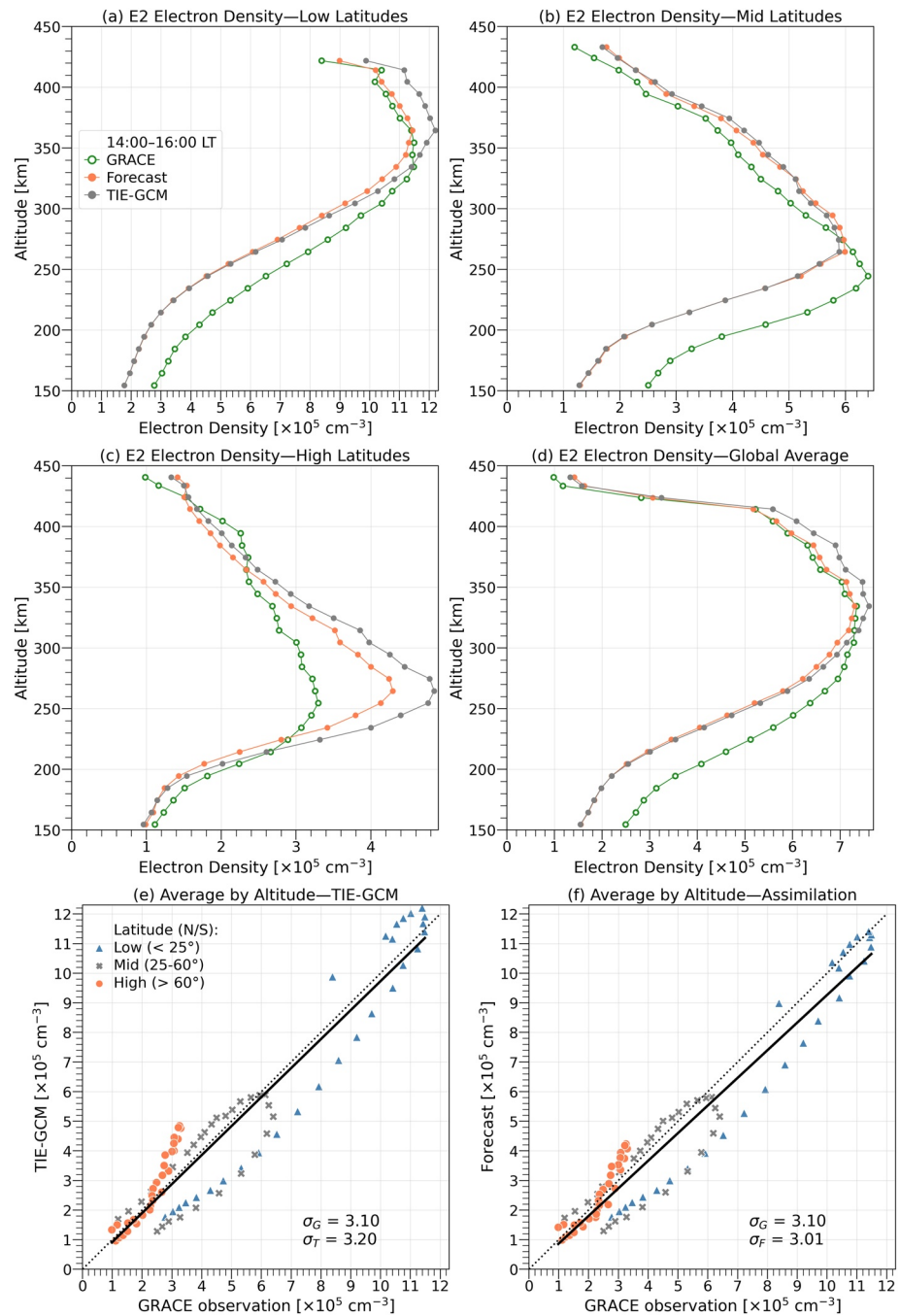
Figure 10. Same as Figure 9 except for E2 at the 14–16 local time sector.

of 250 km. In the middle latitudes, in altitudes approximately above (below) 250 km, both TIE-GCM and forecast seem to significantly overestimate (underestimate) electron densities relative to GRACE data. Figure 9c shows good agreement between TIE-GCM, forecast, and GRACE data in the high latitudes. A slight underestimation of electron density is also apparent in Figure 9c in altitudes below approximately 200 km. The global average electron density profiles in Figure 9d show that the electron density at the F-region peak of the forecast seems to agree well with GRACE data compared to that of TIE-GCM. However, the height of the peak electron density of the forecast in this LT sector shows no visible deviation from that of TIE-GCM. In general, the COSMIC-Ne-guided forecast is shifted toward GRACE data in altitudes above 250 km.

The legend provided in Figure 9e applies to panels 9e and 9f. The results in Figures 9e and 9f show the electron densities averaged per altitude-bin per latitude region (low: blue triangle, middle: gray cross, high: orange dot). The notations σ_G, σ_T, and σ_F refer to the standard deviations (in units of 10^5 cm^{-3}) of GRACE, TIE-GCM, and forecast, respectively, considering the collective distribution across all altitude and latitude bins. Figure 9e shows TIE-GCM's distinctly overestimated and underestimated portions of the distribution relative to GRACE data in low and middle latitudes. Figure 9f clearly shows that much of the adjustment in the forecast correspond to this overestimated portion of TIE-GCM. The overall standard deviation of the forecast is remarkably closer to that of GRACE data.

The presentation in Figure 10 is similar to Figure 9 except for E2 in the 14:00–16:00 LT sector, which corresponds to the LT sampling of GRACE during the E2 time period. The altitude range of the vertical profiles in Figure 10 is less than that of Figure 9 due to GRACE's orbital decay over the years from 2008 to 2014. Figures 10a–10d show that the E2-forecast mostly follows the TIE-GCM control run except for a few notable deviations in the low and high latitudes. In the low latitudes, the E2-forecast is in better agreement with GRACE in altitudes above 300 km. Figure 10b shows that both forecast and TIE-GCM control run severely underestimate electron densities relative to GRACE in the middle latitudes in altitudes below 250 km. The three profiles in Figure 10b are in better agreement with each other in altitudes above 270 km compared to the lower altitudes.

Although the shape of the profiles of forecast and TIE-GCM are similar, the forecast is significantly different from TIE-GCM in the 250–300 km altitude range in the high latitudes in Figure 10c. In Figure 10c, the gradient of the TIE-GCM and forecast profiles in the 230–350 km altitude range appears significantly different from that of GRACE. In this altitude range, both TIE-GCM and forecast significantly overestimate electron densities relative to GRACE. Considering the global average in Figure 10d, the forecast is in better agreement with GRACE in the 300–400 km altitude range but the TIE-GCM is not significantly different from the forecast. The comparison in Figures 10e–10f show that the differences in the respective σ values are only marginal. The two scatter plots clearly visualize that the overall improvement of the E2-forecast in the high latitudes compared to the GPI-driven TIE-GCM control run. Figures 10e–10f demonstrate that while the forecast has largely corrected for overestimation in TIE-GCM relative to GRACE, the underestimation of TIE-GCM relative to GRACE has not changed much in the forecast.

6. Influencing the Neutral Dynamics Through Assimilating COSMIC-*Ne*

This section investigates the impact of assimilating COSMIC-*Ne* on neutral mass density in the thermosphere. Figures 11 and 12 demonstrate this impact on the assimilation runs relative to TIE-GCM and Eval-NA, respectively. The supporting information provides some additional comparisons by local time, altitude, and latitude (Figures S18–S25 and Table S1). Here the objective is to demonstrate the capability of the assimilation scheme to impact the neutral mass density state via assimilating COSMIC-*Ne*. A validation of the resulting neutral mass density is beyond the ambit of the present work but an important future task.

Figure 11 demonstrates an example of this impact on neutral mass density states of E1 (see Figures S15–S17 for additional examples from E1 and E2). The snapshot in Figure 11 corresponds to 3 UT on March 7, 2008. Figures 11a–11c show the neutral mass density estimates from TIE-GCM, forecast, and analysis, respectively. Figures 11d (11e) shows the percentage deviation of forecast (analysis) from TIE-GCM, and Figures 11f shows the percentage deviation of forecast from the analysis. The locations of assimilated COSMIC-*Ne* profiles at the specified altitude within −2.5 and 0.5 h of the specified time are marked with a blue dot.

The most notable feature of Figure 11 is the localized impact to the neutral mass density state apparent in proximity to the locations of COSMIC-*Ne* observations. For example, Figures 11e illustrates that the assimilation of COSMIC-*Ne* has effectively increased the neutral mass density by about 10% in the analysis in the region between approximately 45–75°N and 150–180°E in comparison to TIE-GCM. The comparison around 45°S and 150°W in Figures 11e also shows a signature of this increase in neutral mass density due to assimilation. Figures 11d and 11e illustrate global differences between the forecast and analysis, and GPI-driven TIE-GCM. Some of these differences are accentuated mostly in the terminator regions and high latitudes, and could be mainly attributed to the differences in the solar and geomagnetic forcing between the assimilation runs and TIE-GCM.
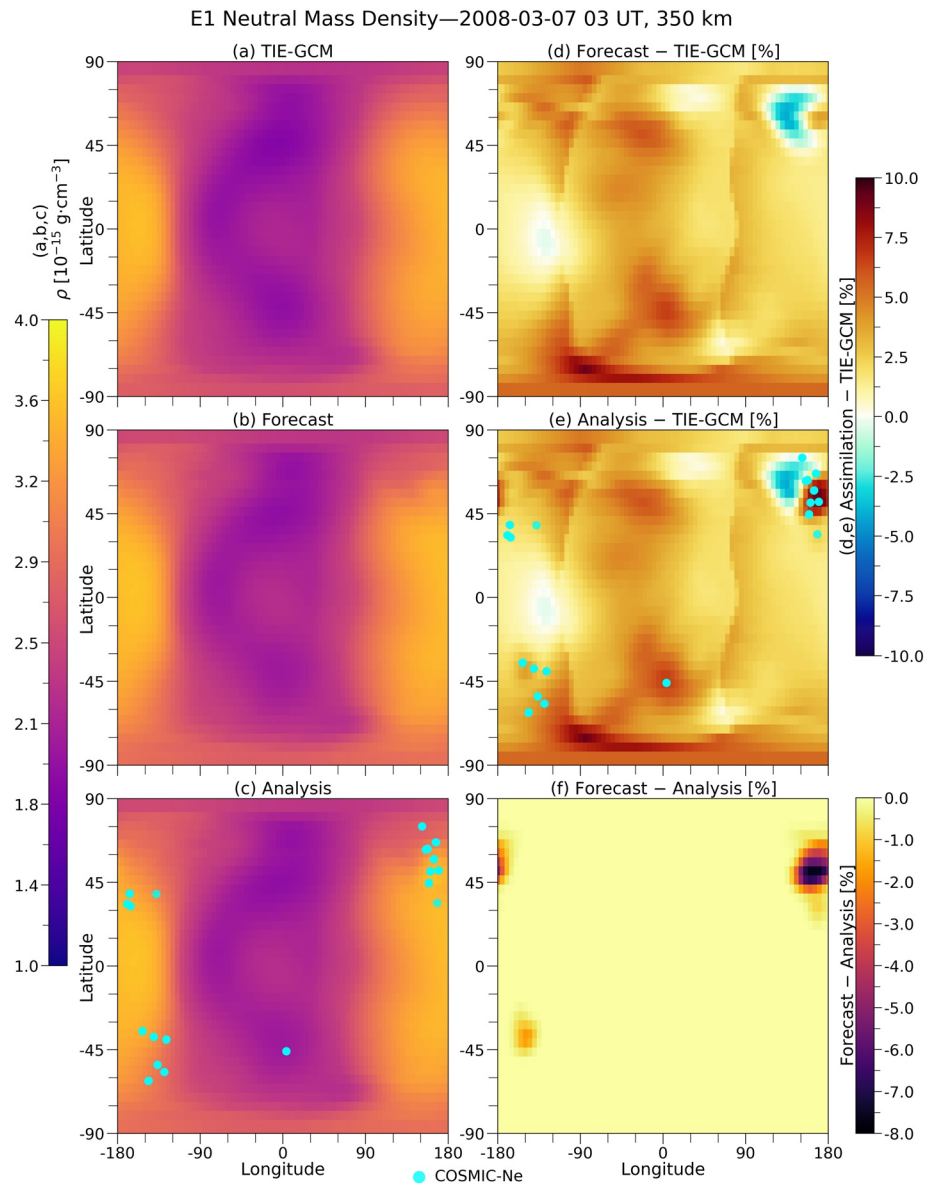
Figure 11. A snapshot of the impact of the assimilation of COSMIC-*Ne* on neutral mass density (ρ) for E1 at the specified time and altitude. The color-bar on the left indicates the magnitude of the geographic longitude-latitude distribution of ρ for (a) TIE-GCM, (b) forecast, and (c) analysis. The color-bar on the top-right shows the percentage difference between (d) forecast and TIE-GCM, and (e) analysis and TIE-GCM. (e) The percentage difference between forecast and analysis. The blue dots indicate the locations of assimilated COSMIC-*Ne* profiles at the specified altitude within −2.5 and 0.5 h of the specified time.

The differences between neutral mass density states of the assimilation runs (analysis and forecast) and nonassimilation run (Eval-NA) yields a direct measure of the impact of the assimilation. Figure 12 presents the ratio of the natural logarithm of neutral mass densities of analysis and forecast relative to Eval-NA (see Section 3.4). In Figure 12, a ln-ratio of zero indicates that the respective assimilation run is not different from Eval-NA. The positive (negative) ratios indicate that the neutral mass density of the respective assimilation run is larger (smaller) than that of Eval-NA. As the background external forcing is identical between analysis, forecast, and Eval-NA, the differences present in Figure 12 is entirely due to the impact of the assimilation of COSMIC-*Ne*.
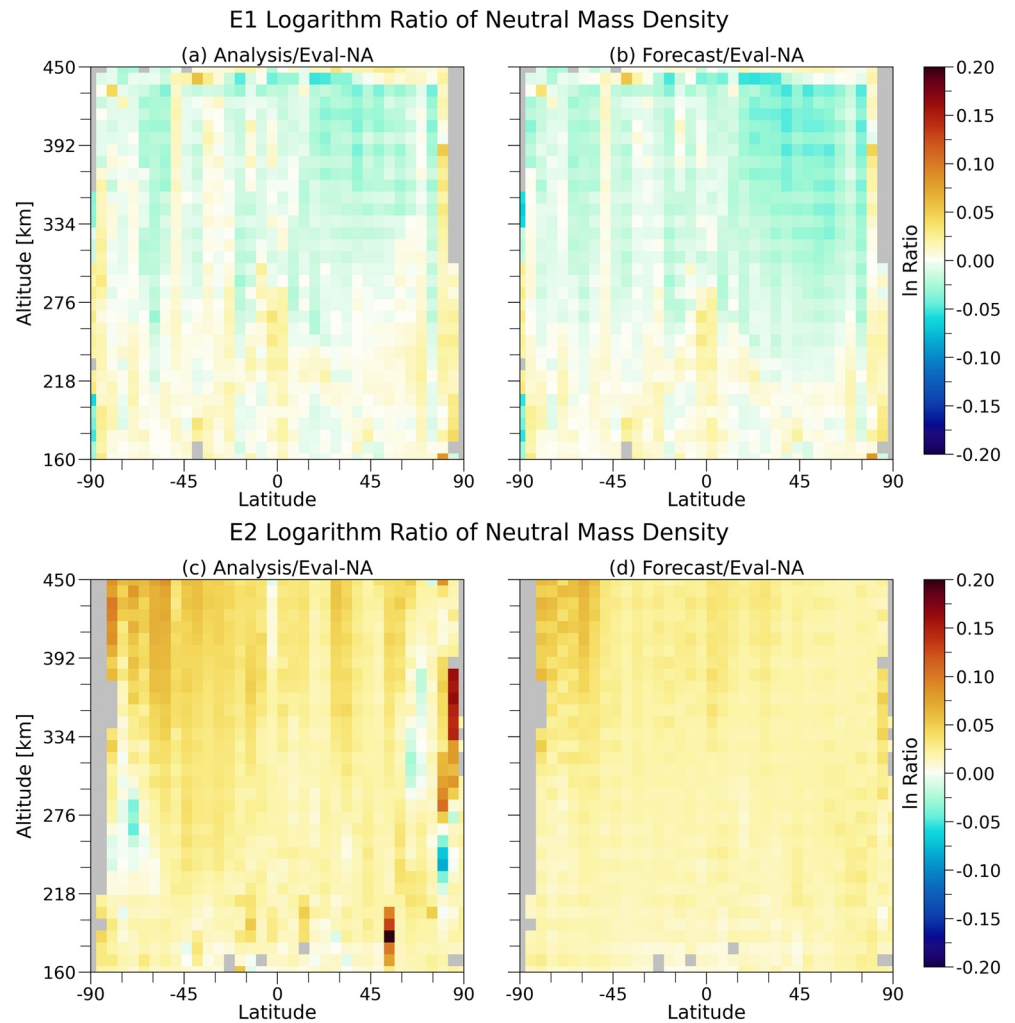
Figure 12. Ratio of the natural logarithm (ln) of neutral mass densities of (a), (c) analysis, and (b), (d) forecast to Eval-NA. The results here represent the longitudinal average as a function of geographic latitude and altitude for experiments (a), (b) E1, and (c), (d) E2.

In general, results for E1 in in Figure 12 show that assimilation of COSMIC-Ne has forced the analysis and forecast to reduce neutral mass densities in altitudes above approximately 300 km. The regions where these differences are prominent correspond well with the regions where model bias differences between electron densities in Eval-NA and assimilation runs are present in Figure 6. Figures 12a and 12b show that, in general, E1-forecast has slightly larger differences with Eval-NA compared to E1-analysis (e.g., above 300 km in northern latitudes). This may be due to the differences in model's physical computation of neutral mass density influenced by altered electron density and other variables in the state vector (see Section 3.2) in a previous assimilation cycle versus statistically updating the neutral mass density in the analysis step.

Figure 12d shows that differences between E2-forecast and Eval-NA does not vary significantly across all altitudes except, for example, in the region around 400 km and south of approximately 60°S. Such features are similar for the E2-analysis in Figure 12c but with some significantly large differences in a few areas (e.g., dark red patch north of 75°N). The pattern of neutral mass density differences in Figure 12c share some similarities with the electron density bias differences present between Figures 7b and 7c. For example, the electron density of E2-analysis in the region corresponding to the above-mentioned dark red patch is significantly higher than that of Eval-NA. Interestingly, Figures 7c and 7d also do not show much difference between Eval-NA and forecast for the bias in electron density. Section 7 discusses these features in detail.

7. Discussion

The results of the present study show that the data assimilation scheme significantly improves the agreement between the analysis and assimilated COSMIC data (see Table 1). The impact of assimilating COSMIC-*Ne* during E1 solar minimum is, in general, consistent with previous similar investigations in, for example, Lee et al. (2012), Matsuo et al. (2013), and Hsu et al. (2014). The relative impact of the assimilation of COSMIC-*Ne* on the analysis state is much more significant during E2 solar maximum than E1 solar minimum (e.g., Figures 6 and 7). The agreement between forecast and COSMIC-*Ne* is better during solar minimum compared to that of solar maximum (see Table 2). Although E1 and E2 belong to two different seasons (March-equinox and June-solstice months), the model bias due to season in TIE-GCM is less compared to the model bias due to GPIs (e.g., Emmert et al., 2014). A companion manuscript in preparation discusses in detail the issue of seasonal bias in data assimilation results.

Lee et al. (2012) report a globally averaged difference of 5% between the forecast and analysis during solar minimum in Figure 1 of their experiment with assimilation of COSMIC-*Ne* for a period of 1 day. The results of the present study based on statistics of two four-day assimilation experiments (E1 and E2) demonstrate that the impact on the model state due to assimilation of COSMIC-*Ne* and thus the differences between the forecast and analysis vary significantly in local time, altitude, latitude, and solar activity. One contributing factor for the differences in the forecasts of Lee et al. (2012) and this study could be the inclusion of O^+ as part of the state vector in this study. Hsu et al. (2014) show in their experiments using synthetic data that the impacts of updating O^+ in the state vector could last for about 10 h.

The comparisons in the observation-space (e.g., Figures 4 and 8) and with independent data (e.g., Figures 9 and 10) show that assimilating COSMIC-*Ne* can also significantly adjust the model forecasts similar to OSSEs with synthetic COSMIC-*Ne* in Hsu et al. (2014). Matsuo et al. (2013) show in their Figure 3 that the impact of assimilation of synthetic COSMIC-*Ne* on neutral mass density forecast state is not significant during solar minimum. Matsuo et al. (2013) also do not include O^+ in their state vector. The results of the present study show that assimilation of COSMIC-*Ne* significantly impacts both electron density and neutral mass density states of the analysis and forecast during both solar minimum and maximum—with some differences in performance between the two periods. The relative impact of the assimilation of COSMIC-*Ne* on neutral mass density is larger during solar maximum compared to solar minimum (see Figure 12). The results also suggest that this impact on neutral mass density state persists through to forecast state better during solar minimum compared to solar maximum (see Figure 12).

The patches of large differences corresponding to E2-analysis in Figure 12c perhaps indicate an artifact due to statistically updating the neutral mass density based on assimilated electron density in the analysis step. Such artifacts could arise due to inaccurate correlations between electron density and the state vector. The E2-forecast seems to suppress these localized differences. This may be due to background solar radiation dominating the interaction between neutrals and ions/electrons via ionization, dissociation, and excitation. In other words, the relatively large insolation during solar maximum compared to solar minimum dampens the influence of localized changes to the state vector on neutral dynamics in the forecast step. Solar radiation controls the overall temperature in the upper atmosphere. The influence of localized enhancements to electron density on neutral dynamics becomes prominent relative to background forcing. For example, in auroral regions, precipitating electrons enhance ionization and thus increase Joule heating, which impart further variability on neutrals. In TIE-GCM, *Ne* is one of the main factors of ion drag force due to the ion-electron quasi-neutrality in the ionosphere. Thus, assimilated *Ne* could introduce variations to neutral temperature, winds as well as a whole range of model dynamics in addition to statistical updates to unobserved variables in the state vector. This further emphasizes the important role of ion-neutral coupling and criticality of correct specification of plasma-neutral interactions in models. Hsu et al. (2016), using TIE-GCM, shows that relatively small errors in temperature can lead to relatively large errors in neutral mass density. These results motivate further experiments to determine whether the benefit of updating also the forcing parameters, such as $F_{10.7}$ in addition to the aforementioned state vector, is more during solar maximum compared to solar minimum.

The comparisons between E1 and E2 reveal the differential model bias during the two vastly different solar activity periods. For example, the local time and latitude dependent performance characteristics highlighted

in Figures 2–3 and Figures 4–5, and summarized in Tables 1 and 2. Figures 5 and 7 demonstrate that data assimilation successfully corrects a known systematic bias of TIE-GCM in the northern summer high latitudes (e.g., Yue et al., 2013). The results of this study also demonstrate that the performance of the forecast with this assimilation scheme is significantly affected during E2 solar maximum. Elvidge et al. (2016) reported that the neutral mass density forecast skill of TIE-GCM is significantly better during the solar minimum than the solar maximum. Although the performance of E2-forecast is relatively worse than the E1-forecast, the $|\sigma_M - \sigma_C|$ results in Table 1 indicate that the assimilation scheme causes considerable changes to the forecast distribution.

The results in Table 2 also help to narrow down the most problematic regions for forecasting during E2: middle (high) latitudes in the 250–350-km (350–450-km) altitude range. Figure 8 shows that TIE-GCM is prone to significantly underestimate electron densities in the middle latitudes relative to COSMIC-*Ne*. These statistics along with diagnostics in supporting information for different latitude regions suggest that the adjusted/updated state in the analysis is overpowered by other forces in the self-consistent model in the middle and high latitudes. For example, Figure S6 show that in altitudes above 250 km, the forecast consistently struggle to converge in the middle latitudes at all local times. Similarly, in Figure S7, in altitudes above 200 km in the high latitudes, the forecast consistently struggle to converge in the nighttime but shows a slight improvement during daytime in the 250–350-km altitude range. Further investigations into this issue in the middle and high latitudes could help identify possible pathways to make useful impact on the forecasted state during high solar activity periods.

This study assesses the accuracy of the forecast state with independent GRACE data. Figures 9 and 10 show that the agreement between forecast and GRACE data during E1 and E2 is in general better than that of GPI-driven TIE-GCM control run. Figure 9 shows no appreciable impact of the assimilation on the forecast in altitudes below 250 km. This indicates that the assimilation does not effect change in model dynamics at locations further from where observations were assimilated. The number of observations assimilated in these lower altitudes are smaller compared to that of higher altitudes. Although the forecast shows a shift toward GRACE data in altitudes above 250 km in low and middle latitudes, the results in Figures 9a and 9b show that the forecast does not change the height of the maximum electron density relative to TIE-GCM control run. This difference in the heights of peak electron densities between GRACE and forecast is about 20 km in the low latitudes and about 30 km in the middle latitudes. Figure S13 provides corroborating evidence for the good correspondence of E1-forecast with GRACE data in low latitudes. Figure S13 shows that forecast has considerably reduced the model bias relative to CHAMP data in the equatorial region. In general, the forecast shows good agreement with CHAMP in-situ measurements in the additional validation in Figures S13 and S14.

The comparison of E2-forecast with GRACE data shows that the impact of the assimilation is mostly noticeable in the high latitudes (see Figure 10). Figure 10 also highlights TIE-GCM's severe underestimation of electron densities in altitudes below 250 km in low and middle latitudes, and significantly different gradient of the profile in the peak electron density region in the high latitudes relative to GRACE data. TIE-GCM's significant overestimation of electron densities in the high latitudes is also apparent relative to COSMIC data in Figure 4e. The results of this study show that this problem of overestimation in the high latitudes is greatly improved in both E2-analysis and -forecast.

The comparison with independent data also gives an indication about the limitations of assimilating COSMIC-*Ne* profiles in an operational setting. While the number of profiles to assimilate can be controlled in experiments with synthetic observations (e.g., Matsuo et al., 2013; Hsu et al., 2014), the availability of bona-fide COSMIC-*Ne* profiles is dependent on multiple factors such as the number of transmitters in view, quality of the receiving radio signals. Only a limited number of observations out of the total available observations gets assimilated in this study due to the outlier threshold as well as the model spread. The quality or the usefulness of, for example, neutral mass density predictions along a given orbit is thus affected by the number of COSMIC observations that fall within a meaningful range (e.g., localization radius) of the respective satellite's path. Here a task will be to ascertain the persistence of the impact of assimilating COSMIC-*Ne* on neutral mass density. For example, if such impact persists for several hours, then a dense enough COSMIC sampling could lead to global changes in neutral mass density, which may benefit applications of neutral mass density predictions.

The impact due to the large errors in COSMIC-*Ne* at altitudes below 200 km (see Section 2) could be mitigated by assimilating the raw slant TEC along the RO ray path. While this would eliminate the dependency on the COSMIC-*Ne* retrieval method, additional errors may be introduced due to needing to extrapolate beyond the top layer of TIE-GCM in the forward operator for slant TEC along the RO ray path. A combination of data sources (e.g., COSMIC, COSMIC-2, and other space- and ground-based measurements) may help improve the limitation with spatial and local time coverage. One possibility is to lower the observational error of COSMIC data, for example, by validating with other in situ or ground-based measurements. The "cleaned-up" COSMIC observations could then be assimilated with a relaxed outlier threshold and lower observational error. The observation rejection ratio could be reduced by increasing the observation error variance—at the cost of observation gain. Although a higher observation error may lower the observation gain, the increase in the number of observations may improve the overall result. Another aspect of caution here is "filter divergence", which is related to the difference between model and observation variances. A large difference between the two variances could lead to filter divergence where the analysis stops converging toward the observation (Anderson, 2001).

8. Summary and Conclusions

This work investigated the response of physics-based TIE-GCM in a data assimilation scheme by assimilating COSMIC electron densities during solar minimum (E1; 4–8 March 2008) and maximum (E2; 2–6 June 2014). With approximately steady solar activity and relatively quiet geomagnetic activity during the two time periods, the two experiments E1 and E2 allowed a comparison of the assimilation results at different solar activity levels. COSMIC, among others, represents one of the largest databases of ionospheric electron density. This work represents the first comprehensive comparison of the impact of solar activity on forecasting the upper atmosphere through assimilation of COSMIC electron densities into TIE-GCM. This work compared the assimilated quantity electron density and its impact on neutral mass density in the thermosphere. The results are not only useful to gauge the accuracy of the assimilation, to explain the inherent model bias, and to understand the limitations of the data, but they also demonstrate the capability of the assimilation technique in the presence of realistic data assimilation scenarios to forecast the highly dynamical thermosphere.

The results showed that the data assimilation scheme significantly improves the agreement between the analysis and assimilated COSMIC data. On the one hand, the impact of the assimilation on the analysis/posterior *Ne* state was much more significant during solar maximum compared to the solar minimum. On the other hand, the agreement between forecast/prior *Ne* and COSMIC data was better during solar minimum compared to that of solar maximum. This study assessed the accuracy of the forecast states with independent GRACE data. The results showed that forecast is mostly better than the GPI-driven TIE-GCM control run. The results emphasized that TIE-GCM significantly underestimate electron density in low altitudes (mostly below 250 km) and the assimilation of COSMIC data is not as effective in these lower altitudes compared to higher altitudes.

The results also demonstrated that assimilation of COSMIC-*Ne* significantly impacts neutral mass density states of the analysis and forecast during both solar minimum and maximum. The relative impact on neutral mass density is larger during solar maximum compared to solar minimum. However, the impact of assimilation of COSMIC-*Ne* on neutral mass density state persists through to forecast state better during solar minimum compared to solar maximum. The results suggested that COSMIC data may be utilized in applications of neutral mass density forecasts (e.g., satellite orbit prediction). Further experiments are needed to understand the challenges of such operational ensemble prediction systems.

The experiments mainly focused on the assimilation accuracy during two different solar activity periods. More work needs to be done to identify and improve model bias due to external forcing—especially high solar activity above 120 sfu. More specifically, research into the impact of external forcing on the persistence skill of these forecasts will be useful, among others, to enhance our current forecasting capabilities. Assimilation of other data, for example, ground-based remote sensing measurements of thermospheric neutral winds and temperature could also help unravel some difficulties associated with forecasting the upper atmosphere.

Data Availability Statement

The UCAR/DART (www.image.ucar.edu/DAReS/DART) provided the data assimilation tools used in this work. The UCAR/HAO (www.hao.ucar.edu/modeling/tgcm) provided the TIE-GCM code. The UCAR COSMIC Data Analysis and Archive Center (cosmic.ucar.edu) provided the level-2 electron density profiles for COSMIC and GRACE. The GFZ Data Services (https://doi.org/10.5880/GFZ.2.3.2019.007) provided the CHAMP electron density data (CH-ME-2-PLPT). The NASA/OMNI database (omniweb.gsfc.nasa.gov) provided the measurements Kp, ap, Dst, and $F_{10.7}$.

References

Anderson, J., Hoar, T., Raeder, K., Liu, H., Collins, N., Torn, R., & Avellano, A. (2009). The data assimilation research testbed: A community facility. *Bulletin of the American Meteorological Society*, *90*(9), 1283–1296. https://doi.org/10.1175/2009BAMS2618.1

Anderson, J. L. (2001). An ensemble adjustment Kalman filter for data assimilation. *Monthly Weather Review*, *129*(12), 2884–2903. https://doi.org/10.1175/1520-0493(2001)129<2884:aeakff>2.0.co;2

Chartier, A. T., Matsuo, T., Anderson, J. L., Collins, N., Hoar, T. J., Lu, G., et al. (2016). Ionospheric data assimilation and forecasting during storms. *Journal of Geophysical Research: Space Physics*, *121*(1), 764–778. https://doi.org/10.1002/2014JA020799

Codrescu, S. M., Codrescu, M. V., & Fedrizzi, M. (2018). An ensemble Kalman filter for the thermosphere-ionosphere. *Space Weather*, *16*(1), 57–68. https://doi.org/10.1002/2017SW001752

Daley, R. (1993). Atmospheric data analysis. In M. J. R. J. AlexanderDessler, & J. T. Houghton (Eds.), Cambridge atmospheric and space science series (Vol. 2). Cambridge University Press. ISBN: 9780521458252.

Dickinson, R. E., Ridley, E. C., & Roble, R. G. (1984). Thermospheric general circulation with coupled dynamics and composition. *Journal of the Atmospheric Sciences*, *41*(2), 205–219. https://doi.org/10.1175/1520-0469(1984)041%E2%9F%A80205:TGCWCD%E2%9F%A92.0.CO;2

Elvidge, S., Godinez, H. C., & Angling, M. J. (2016). Improved forecasting of thermospheric densities using multi-model ensembles. *Geoscientific Model Development*, *9*(6), 2279–2292. https://doi.org/10.5194/gmd-9-2279-2016

Emmert, J. T., McDonald, S. E., Drob, D. P., Meier, R. R., Lean, J. L., & Picone, J. M. (2014). Attribution of interminima changes in the global thermosphere and ionosphere. *Journal of Geophysical Research: Space Physics*, *119*(8), 6657–6688. https://doi.org/10.1002/2013JA019484

Emmert, J. T., & Picone, J. M. (2010). Climatology of globally averaged thermospheric mass density. *Journal of Geophysical Research*, *115*(A9). https://doi.org/10.1029/2010JA015298

Evensen, G. (1994). Sequential data assimilation with a nonlinear quasi-geostrophic model using Monte Carlo methods to forecast error statistics. *Journal of Geophysical Research*, *99*(C5), 10143–10162. https://doi.org/10.1029/94JC00572

Gaspari, G., & Cohn, S. E. (1999). Construction of correlation functions in two and three dimensions. *Quarterly Journal of the Royal Meteorological Society*, *125*(554), 723–757. https://doi.org/10.1002/qj.49712555417

Habarulema, J. B., Katamzi, Z. T., & Yizengaw, E. (2014). A simultaneous study of ionospheric parameters derived from FORMOSAT-3/COSMIC, GRACE, and CHAMP missions over middle, low, and equatorial latitudes: Comparison with ionosonde data. *Journal of Geophysical Research: Space Physics*, *119*(9), 7732–7744. https://doi.org/10.1002/2014JA020192

Hagan, M. E., Roble, R. G., & Hackney, J. (2001). Migrating thermospheric tides. *Journal of Geophysical Research*, *106*(A7), 12739–12752. https://doi.org/10.1029/2000JA000344

Heelis, R. A., Lowell, J. K., & Spiro, R. W. (1982). A model of the high-latitude ionospheric convection pattern. *Journal of Geophysical Research*, *87*(A8), 6339–6345. https://doi.org/10.1029/JA087iA08p06339

Houtekamer, P. L., & Mitchell, H. L. (2001). A sequential ensemble kalman filter for atmospheric data assimilation. *Monthly Weather Review*, *129*(1), 123–137. https://doi.org/10.1175/1520-0493(2001)129%E2%9F%A80123:ASEKFF%E2%9F%A92.0.CO;2

Hsu, C.-T., Matsuo, T., & Liu, J.-Y. (2018). Impact of Assimilating the FORMOSAT-3/COSMIC and FORMOSAT-7/COSMIC-2 RO Data on the Midlatitude and Low-Latitude Ionospheric Specification. *Earth and Space Science*, *5*(12), 875–890. https://doi.org/10.1029/2018EA000447

Hsu, C.-T., Matsuo, T., Wang, W., & Liu, J.-Y. (2014). Effects of inferring unobserved thermospheric and ionospheric state variables by using an ensemble Kalman filter on global ionospheric specification and forecasting. *Journal of Geophysical Research: Space Physics*, *119*(11), 9256–9267. https://doi.org/10.1002/2014JA020390

Hsu, C.-T., Matsuo, T., Yue, X., Fang, T.-W., Fuller-Rowell, T., Ide, K., & Liu, J.-Y. (2018). Assessment of the impact of FORMOSAT-7/COSMIC-2 GNSS RO observations on midlatitude and low-latitude ionosphere specification: Observing system simulation experiments using ensemble square root filter. *Journal of Geophysical Research: Space Physics*, *123*(3), 2296–2314. https://doi.org/10.1002/2017JA025109

Hsu, V. W., Thayer, J. P., Wang, W., & Burns, A. (2016). New insights into the complex interplay between drag forces and its thermospheric consequences. *Journal of Geophysical Research: Space Physics*, *121*(10), 417–10. https://doi.org/10.1002/2016JA023058

Kalman, R. E. (1960). A new approach to linear filtering and prediction problems. *Journal of Basic Engineering*, *82*(1), 35–45. https://doi.org/10.1115/1.3662552

Kalnay, E. (2002). *Atmospheric modeling, data assimilation and predictability*. Cambridge University Press. ISBN: 9780511802270. https://doi.org/10.1017/CBO9780511802270

Lee, I. T., Matsuo, T., Richmond, A. D., Liu, J. Y., Wang, W., Lin, C. H., et al. (2012). Assimilation of FORMOSAT-3/COSMIC electron density profiles into a coupled thermosphere/ionosphere model using ensemble Kalman filtering. *Journal of Geophysical Research*, *117*(A10). https://doi.org/10.1029/2012JA017700

Liu, J.-Y., Lee, C.-C., Yang, J.-Y., Chen, C.-Y., & Reinisch, B. W. (2009). Electron density profiles in the equatorial ionosphere observed by the FORMOSAT-3/COSMIC and a digisonde at Jicamarca. *GPS Solutions*, *14*(1), 75. https://doi.org/10.1007/s10291-009-0150-3

Liu, J. Y., Lin, C. Y., Lin, C. H., Tsai, H. F., Solomon, S. C., Sun, Y. Y., et al. (2010). Artificial plasma cave in the low-latitude ionosphere results from the radio occultation inversion of the FORMOSAT-3/COSMIC. *Journal of Geophysical Research*, *115*(A7). https://doi.org/10.1029/2009JA015079

Matsuo, T., Lee, I.-T., & Anderson, J. L. (2013). Thermospheric mass density specification using an ensemble Kalman filter. *Journal of Geophysical Research: Space Physics*, *118*(3), 1339–1350. https://doi.org/10.1002/jgra.50162

Maute, A. (2017). Thermosphere-ionosphere-electrodynamics general circulation model for the ionospheric connection explorer: TIEGCM-ICON. *Space Science Reviews*, *212*(1), 523–551. https://doi.org/10.1007/s11214-017-0330-3

Mehta, P. M., Linares, R., & Sutton, E. K. (2018). A quasi-physical dynamic reduced order model for thermospheric mass density via Hermitian space-dynamic mode decomposition. *Space Weather*, *16*(5), 569–588. https://doi.org/10.1029/2018SW001840

National Research Council. (2013). *Solar and space physics: A science for a technological society*. National Academies Press. ISBN: 9780309387392. https://doi.org/10.17226/13060

Pedatella, N. M., Liu, H.-L., Marsh, D. R., Raeder, K., Anderson, J. L., Chau, J. L., et al. (2018). Analysis and hindcast experiments of the 2009 sudden stratospheric warming in WACCMX+DART. *Journal of Geophysical Research: Space Physics*, *123*(4), 3131–3153. https://doi.org/10.1002/2017JA025107

Pedatella, N. M., Yue, X., & Schreiner, W. S. (2015). An improved inversion for FORMOSAT-3/COSMIC ionosphere electron density profiles. *Journal of Geophysical Research: Space Physics*, *120*(10), 8942–8953. https://doi.org/10.1002/2015JA021704

Qian, L., Burns, A. G., Emery, B. A., Foster, B., Lu, G., Maute, A., et al. (2014). The NCAR TIE-GCM: A community model of the coupled thermosphere/ionosphere system. In *Modeling the ionosphere thermosphere system* (pp. 73–83). John Wiley. chap. 7ISBN: 9781118704417. https://doi.org/10.1002/9781118704417.ch7

Qian, L., Solomon, S. C., & Kane, T. J. (2009). Seasonal variation of thermospheric density and composition. *Journal of Geophysical Research*, *114*(A1), a. https://doi.org/10.1029/2008JA013643

Richards, P. G., Fennelly, J. A., & Torr, D. G. (1994). EUVAC: A solar EUV flux model for aeronomic calculations. *Journal of Geophysical Research*, *99*(A5), 8981–8992. https://doi.org/10.1029/94JA00518

Richmond, A. D. (1995). Ionospheric electrodynamics using magnetic apex coordinates. *Journal of Geomagnetism and Geoelectricity*, *47*(2), 191–212. https://doi.org/10.5636/jgg.47.191

Richmond, A. D., Ridley, E. C., & Roble, R. G. (1992). A thermosphere/ionosphere general circulation model with coupled electrodynamics. *Geophysical Research Letters*, *19*(6), 601–604. https://doi.org/10.1029/92GL00401

Roble, R. G., & Ridley, E. C. (1987). An auroral model for the NCAR thermospheric general circulation model (TGCM). *Annales Geophysicae - Series A: Upper Atmosphere and Space Sciences*, *5*, 369–382.

Solomon, S. C., & Qian, L. (2005). Solar extreme-ultraviolet irradiance for general circulation models. *Journal of Geophysical Research*, *110*(A10). https://doi.org/10.1029/2005JA011160

Sutton, E. K. (2018). A new method of physics-based data assimilation for the quiet and disturbed thermosphere. *Space Weather*, *16*(6), 736–753. https://doi.org/10.1002/2017SW001785

Tsai, L.-C., Tsai, W. H., Schreiner, W. S., Berkey, F. T., & Liu, J. Y. (2001). Comparisons of GPS/MET retrieved ionospheric electron density and ground based ionosonde data. *Earth, Planets and Space*, *53*(3), 193–205. https://doi.org/10.1186/BF03352376

Yue, X., Schreiner, W. S., Kuo, Y.-H., Wu, Q., Deng, Y., & Wang, W. (2013). GNSS radio occultation (RO) derived electron density quality in high latitude and polar region: NCAR-TIEGCM simulation and real data evaluation. *Journal of Atmospheric and Solar-Terrestrial Physics*, *98*, 39–49. https://doi.org/10.1016/j.jastp.2013.03.009

Yue, X., Schreiner, W. S., Lei, J., Sokolovskiy, S. V., Rocken, C., Hunt, D. C., & Kuo, Y.-H. (2010). Error analysis of Abel retrieved electron density profiles from radio occultation measurements. *Annales Geophysicae*, *28*(1), 217–222. https://doi.org/10.5194/angeo-28-217-2010

Yue, X., Schreiner, W. S., Pedatella, N., Anthes, R. A., Mannucci, A. J., Straus, P. R., & Liu, J. Y. (2014). Space Weather Observations by GNSS Radio Occultation: From FORMOSAT-3/COSMIC to FORMOSAT-7/COSMIC-2. *Space Weather*, *12*(11), 616–621. https://doi.org/10.1002/2014SW001133